

SegVol: Universal and Interactive Volumetric Medical Image Segmentation

Yuxin Du¹, Fan Bai^{1,2}, Tiejun Huang^{1,3}, Bo Zhao^{1†}

¹Beijing Academy of Artificial Intelligence

²The Chinese University of Hong Kong ³Peking University

[†]Corresponding author: Bo Zhao <bozhaonanjing@gmail.com>

Abstract

Precise image segmentation provides clinical study with instructive information. Despite the remarkable progress achieved in medical image segmentation, there is still an absence of 3D foundation segmentation model that can segment a wide range of anatomical categories with easy user interaction. In this paper, we propose a 3D foundation segmentation model, named SegVol, supporting universal and interactive volumetric medical image segmentation. By scaling up training data to 90K unlabeled Computed Tomography (CT) volumes and 6K labeled CT volumes, this foundation model supports the segmentation of over 200 anatomical categories using semantic and spatial prompts. Extensive experiments on 10 internal validation tasks and 18 external validation tasks verify that SegVol outperforms the state of the art by a large margin. Through its capacity to provide precise volumetric segmentation across various anatomical categories, SegVol has the potential to accelerate advancements in medical imaging diagnosis and facilitate treatment optimization. The model and code are publicly available at: <https://github.com/BAAI-DCAI/SegVol>.

1. Introduction

Volumetric image segmentation, involving extracting 3D regions of interest, such as organs, lesions, and tissues, plays a pivotal role in medical image analysis by accurately modeling the 3D structural information of the human body from volumetric medical images such as CT or MRI. This technique benefits numerous clinical applications including tumors monitoring [51, 62], surgical planning [12, 41], disease diagnosis [4], therapy optimization [52, 68], etc.

Compared to 2D medical image segmentation [5, 13, 25, 42, 57, 67, 69, 70, 72], volumetric image segmentation is notably more challenging due to the labor-intensive annotation and resource-consuming computation. The research of volumetric medical image segmentation has garnered substantial attention, leading to a series of advancements

[15, 16, 24, 33, 61, 71]. However, there exist several key limitations of the above-mentioned methods, which prevent their application in challenging tasks, e.g., liver tumor or colon cancer segmentation [2, 7, 14, 43], and real-world tasks, e.g., human-interactive segmentation [23, 31, 38, 46]. Firstly, the publicly available volumetric medical image datasets usually consist of a small number of mask annotations from a few varying categories. Due to the different label spaces, the traditional task-specific segmentation models trained on one dataset have difficulty in generalizing to others. For example, the CT-ORG dataset [2, 8, 47, 48] contains ‘lungs’ category, while this category is split into two sub-classes and named ‘left lung’ and ‘right lung’ in the LUNA16 dataset [54]. The main reason is that these models do not understand the semantics of anatomical categories. Secondly, traditional segmentation models have inferior performance when segmenting complex structures, such as tumors and cysts [27]. This is because these models are trained on insufficient data and are also not able to leverage the spatial information through user interaction. Thirdly, previous solutions are computationally expensive in the inference process. They typically employ a sliding window to infer the whole volumetric input. This strategy is not only time-consuming but also short-sighted, as the sliding window contains only local information. Recently, there have been some works [6, 38, 64] that introduce spatial prompts into medical image segmentation. However, most of them lack the ability to process the 3D input directly, e.g. [6, 38], and none of them is able to understand the semantics of anatomical categories.

Motivated by the success of 2D image analysis [31, 38], we present the first foundation model, *SegVol*, for volumetric medical image segmentation. SegVol enables universal and interactive segmentation of more than 200 anatomical categories, supporting both spatial and semantic prompts. SegVol is built on a lightweight architecture, ensuring its efficiency for practical medical image analysis. We summarize the key features of SegVol as follows:

1. Implement the massive pre-training on 96K CT vol-

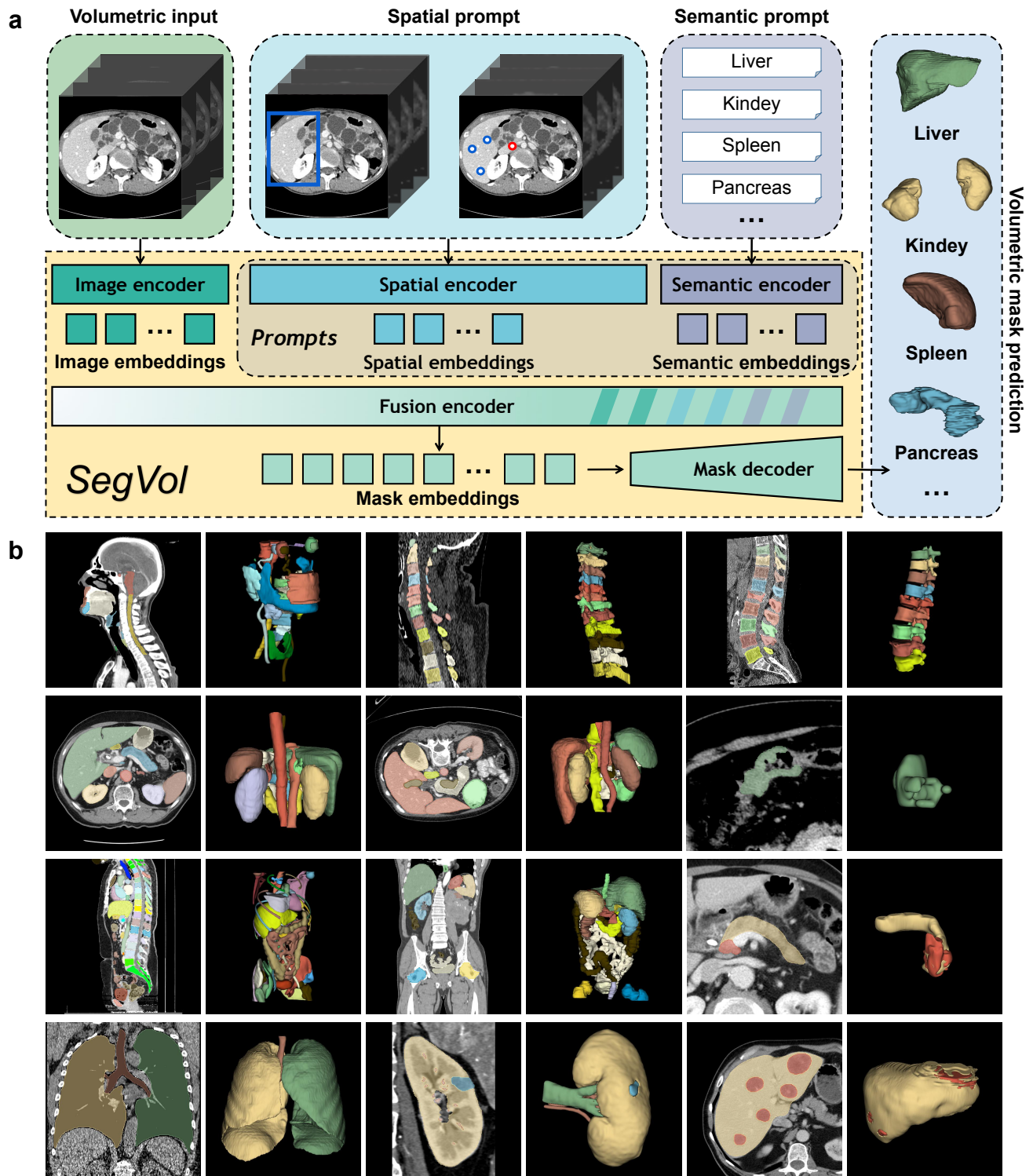


Figure 1. **Overview of the model architecture and representative samples in the joint dataset.** **a.** SegVol can model the 3D anatomical structures from volumetric inputs with easy user interactions including bounding box, point and text prompts. **b.** The joint dataset encompasses various anatomical structures in major regions of the human body. Several volume examples are demonstrated as 2D slices and 3D shapes in the images respectively.

umes and the supervised fine-tuning on 25 public volumetric medical image segmentation datasets.

2. Enable semantic-prompt segmentation on over 200 anatomical categories by integrating the language model into the segmentation model.
3. Employ a synergistic mechanism to coordinate the spatial-prompt and semantic-prompt in the model and achieve high-precision segmentation.
4. Design a zoom-out-zoom-in strategy that significantly reduces the computational cost, meanwhile preserving precise segmentation.

We extensively evaluate the proposed SegVol on 10 internal validation tasks and 18 external validation tasks, which encompass a variety of anatomical structures including organs, tissues, and lesions. The internal validation experiments show that SegVol outperforms the traditional task-specific segmentation models, and the external validation experiments demonstrate that our method surpasses the state-of-the-art interactive models by a large margin. These experimental results verify the capabilities of SegVol as a foundation model for universal and interactive volumetric medical image segmentation.

2. Results

2.1. SegVol: a 3D foundation model for volumetric medical image segmentation

It is a long-standing challenge in medical image analysis to build a 3D foundation model that is capable of handling a wide range of segmentation tasks while achieving precise segmentation results. This challenge has two critical aspects. On the one hand, volumetric medical imaging datasets are usually dispersed and small in scale, making it challenging to train a comprehensive 3D foundation model that can generalize well across diverse datasets. On the other hand, segmentation tasks in medical image analysis encompass a wide range of semantic categories and spatial scales, ranging from organ to lesion segmentation, further complicating the development of a general solution.

To establish a universal volumetric segmentation model proficient in multiple tasks, we collect 25 CT volume segmentation datasets from public medical datasets and process them into a joint dataset, involving popular segmentation tasks. A total of 5,772 CT volumes of the joint dataset participate in the training and internal validation, with 149,199 volumetric masks and semantics. The collected joint dataset includes major regions of the human body, i.e., the head, neck, thorax, abdomen, and pelvis, comprising over 200 categories of organs and tissues, and 28 lesion tasks from different benchmarks. Some representative samples are shown in Fig. 1 b. The detailed information of joint dataset can be obtained from Supplementary Tables 1, 2, and Fig. 2.

Developing a universal segmentation model is challenging due to two main obstacles. One is the large number of categories leading to ambiguous semantics, where the same voxel may correspond to multiple targets. Another obstacle lies in the wide range of spatial scales of targets, varying from small lesions to large organs, and the complex and diverse structures of targets in the space. To address these challenges, our method adopts innovative strategies demonstrated in Fig. 1 a. As a universal model, our approach delivers accurate segmentation results for over 200 important organs, tissues, and lesions by leveraging text prompts to clarify semantic references. Furthermore, as a precise segmentation model, SegVol introduces point and bbox(bounding box) spatial prompts to guide the segmentation of anatomical structures, thus achieving high-precision segmentation performance. By leveraging these techniques, our method navigates the ambiguous semantics arising from numerous categories and accommodates the varying spatial scales and complex structures of targets, ensuring robust and precise segmentation across a wide range of medical imaging tasks.

2.2. Internal validation compared with task-specific segmentation models

Task-specific segmentation models mainly fall into two architectures, CNN-based models and Transformer-based models. We conduct internal comparative experiments with representative CNN-based models i.e. 3DUX-Net [33] and nnU-Net [24], and representative Transformer-based models i.e. SwinUNETR [15]. We conduct internal validation experiments on the test set of joint dataset, which is not observed during the training phase of SegVol. The 10 internal segmentation tasks are selected from BTCV [32] and MSD-spleen [58] datasets, which focus on organ segmentation, and from MSD-lung, MSD-colon, and MSD-liver datasets, which focus on lesion segmentation. We train task-specific segmentation models on each dataset individually for each method.

The quantitative experimental results are summarized in Fig. 2 a. Generally speaking, SegVol, jointly trained on 25 datasets, outperforms traditional task-specific segmentation models trained on a single dataset. Compared to these strong baselines, SegVol exhibits a narrower distribution of DSC scores across the eight tasks, indicating its robustness and good generalization ability. This mainly owes to the massive knowledge learned from diverse samples of the same categories but different datasets. SegVol depicts excellent performance on lesion tasks which are more challenging in semantic understanding and spatial locating. We present a detailed comparison to nnU-Net [24] on lesion tasks. As shown in Fig. 2 c, the average Dice score of SegVol is 14.76% higher than that of nnU-Net for lesion tasks. We visualize the prediction results of the two methods in Fig. 2 d, which intuitively show that SegVol performs more precise segmentation of the tumors than nnU-Net. The detailed

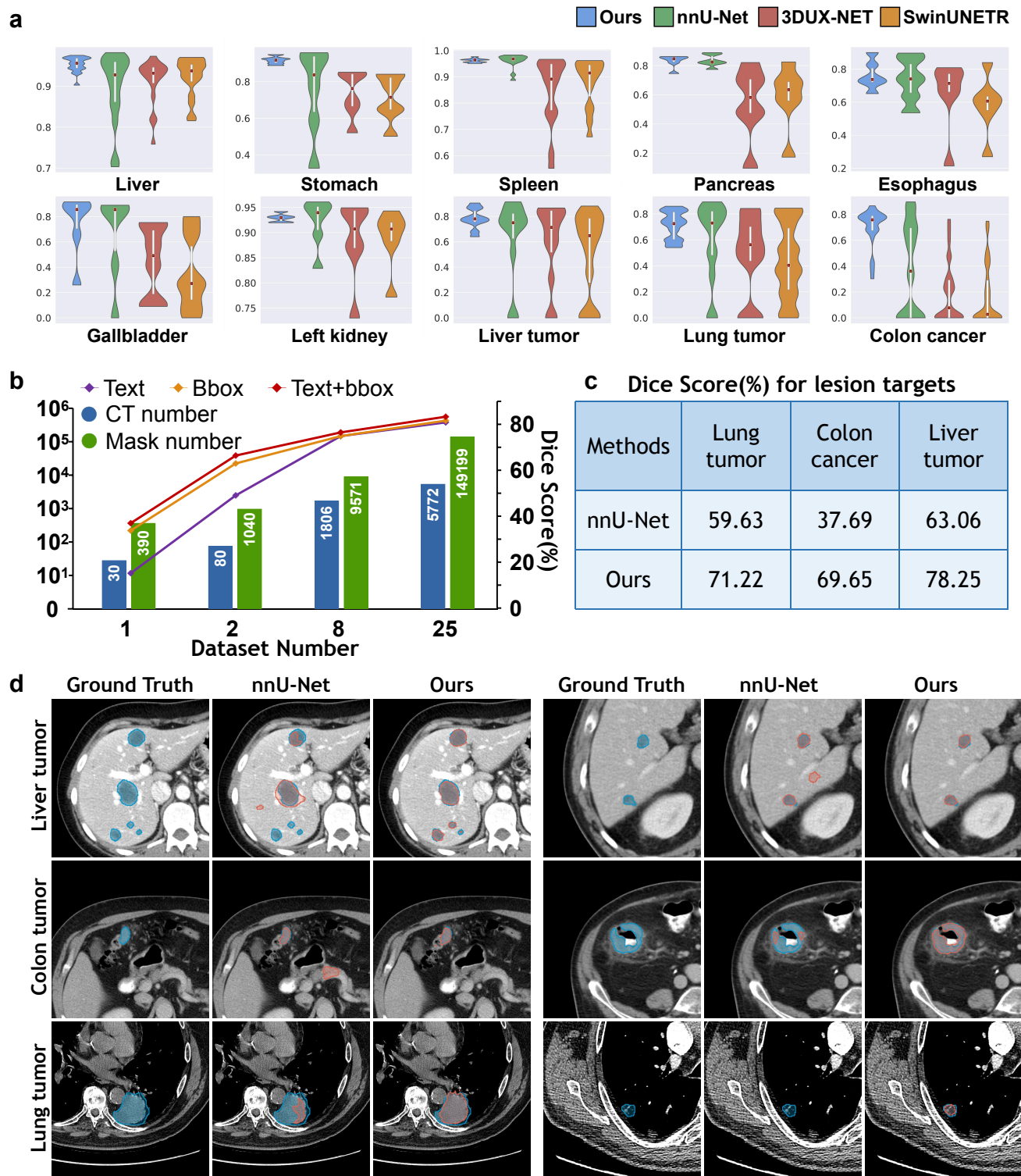


Figure 2. **Quantitative results and visualization of internal validation experiments.** **a.** Violin plots for comparing experiment results of SegVol and task-specific methods. The vertical axis is the Dice score. **b.** The performance of SegVol improves as the training dataset scales up. **c.** The comparison of the average Dice score of SegVol and nnU-Net [24] across 3 internal lesion tasks. **d.** Visualization results of SegVol and nnU-Net across 3 internal lesion tasks.

scores and visualization results of interval validation are presented in Supplementary Table 3 and Fig. 3-5.

We analyze that there are mainly three factors that make SegVol more powerful than traditional task-specific models: 1) Massive generative pre-training on unlabeled data endows SegVol with a complete understanding of the volumetric structures and the discriminative feature representations, which is much superior to learning from a small number of samples. 2) Learning from joint datasets with semantic prompts makes SegVol generalize better to unseen data and categories. For instance, SegVol can learn from both ‘left kidney’ and ‘kidney’ categories based on their semantic correlation, while traditional task-specific models treat the two categories independently. 3) SegVol can be prompted with (spatial) points/bboxes, which provide a precise spatial reference, and (semantic) texts, which disambiguate the overlap of multiple categories in the same space. In contrast, traditional methods are not able to understand semantics. This ability enables SegVol to perform better than traditional methods in challenging tasks, e.g., segmenting lesions.

2.3. External validation compared with interactive methods

Several efforts have been made to construct an interactive segmentation model. However, some of these works, such as MedSAM [38] and SAM-MED2D [6], focus on 2D tasks and cannot process 3D input directly. The other 3D-based methods, such as SAM-MED3D [64], only support small cropped input and lack semantic information support, which is still far from building a comprehensive foundation model for volumetric medical image analysis. To compare with these interactive segmentation models, we performed external validation experiments on 1,738 cases from the validation set of AMOS22 [26] and the whole novel annotated set of Universal Lesion Segmentation Challenge 23(ULS23) [9]. The validation set of AMOS22 contains 120 cases annotated with 15 main organs. The novel annotated ULS23 dataset is composed of three subsets, namely, DeepLesion3D, Radboudumc Bone, and Radboudumc Pancreas. The DeepLesion3D subset contains 200 abdominal lesions, 100 bone lesions, 50 kidney lesions, 50 liver lesions, 100 lung lesions, 100 mediastinal lesions, and 150 assorted lesions cases. There are 744 bone lesion cases in the Radboudumc Bone subset and 124 pancreas lesion cases in the Radboudumc Pancreas subset.

The quantitative results of external validation experiments are shown in Fig. 3. The Fig. 3 a illustrates our method is the best in most of the tasks including lesions and organs, compared to other SAM-like interactive models. MedSAM [38] and SAM(bounding box) [31] use bounding box prompts. SAM(5 clicks) [31], SAM-MED2D [6] and SAM-MED3D [64] use point prompts and a five-step correction procedure, which means that the point prompt in each step will be given according to the previous-step output

and ground truth, rather than giving all at once. In this experiment, our SegVol uses bounding box and text prompt which performs better than other kinds of prompt combinations. We provide the ablation study in Fig. 3 b, which shows the good performance of SegVol among different prompt types, especially bbox(bounding box) prompt and text+bbox prompt. Note that the category of each mask in ULS23 is not clearly defined. Thus, we give a general text (i.e. ‘tumor’ or ‘lesion’) to prompt SegVol, and it is compatible with such general prompts and performs well. The detailed scores and visualization results of external validation are presented in Supplementary Table 5 and Fig. 6-8.

In Fig. 4, we visualize the segmentation results in 4 important organ categories to study the differences within these interactive models. Due to the lack of understanding of the 3D structure, 2D methods like MedSAM and SAM(bbox) present worse results. Although the 3D segmentation method, SAM-MED3D, performs well in the easy aorta case, it demonstrates poor segmentation results in others, especially the pancreas and stomach cases. SegVol achieves good segmentation results stably in all categories, relying on its full understanding of 3D spatial structures and semantics.

In addition, we discuss the generalization performance of SegVol on an external MRI dataset. We collect 60 MRI scans annotated with 4 key organ categories from CHAOS [28–30] dataset and evaluate the generalization ability to unseen modality of SegVol. It achieves median Dice scores of 85.70%, 80.09%, 80.04%, and 81.46% for liver, spleen, left kidney, and right kidney, respectively. This generalization result demonstrates the robustness of SegVol in the face of completely unseen modality data. The detailed scores and visualization results are presented in Supplementary Table 4 and Fig. 9.

2.4. The interaction relationship between spatial-prompt and semantic-prompt

As a universal model, our approach achieves precise segmentation for over 200 organs, tissues, and lesions using both spatial and semantic prompts. In Fig. 5 a, we quantitatively analyze the mutually supportive relationship between semantic-prompt and spatial-prompt in 19 internal segmentation tasks. On the one hand, spatial prompts allow the model to locate the specific part in the 3D space. According to Fig. 5 a, the average Dice score of ‘bbox+text’ prompt is boosted by 5.85% compared to the ‘text’ prompt on average. On the other hand, semantic prompts clarify the reference to the anatomical structure, eliminating the ambiguity of spatial prompts and the plausible masks of multiple categories. This is reflected in Fig. 5 a as the average Dice score of ‘point+text’ prompts is 4.62% higher than using ‘point’ prompts alone. Spatial and semantic prompts mutually support each other, ultimately endowing the model with powerful segmentation capabilities.

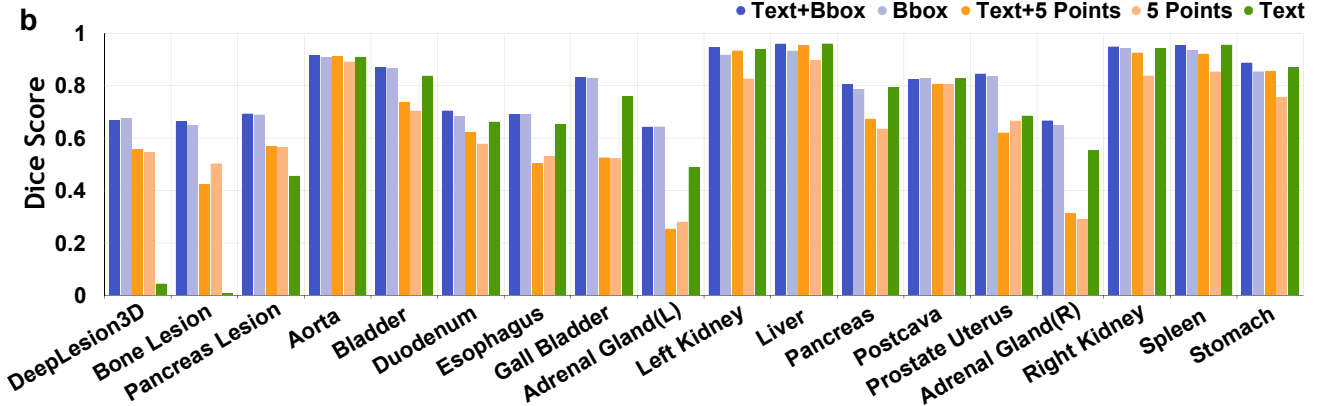
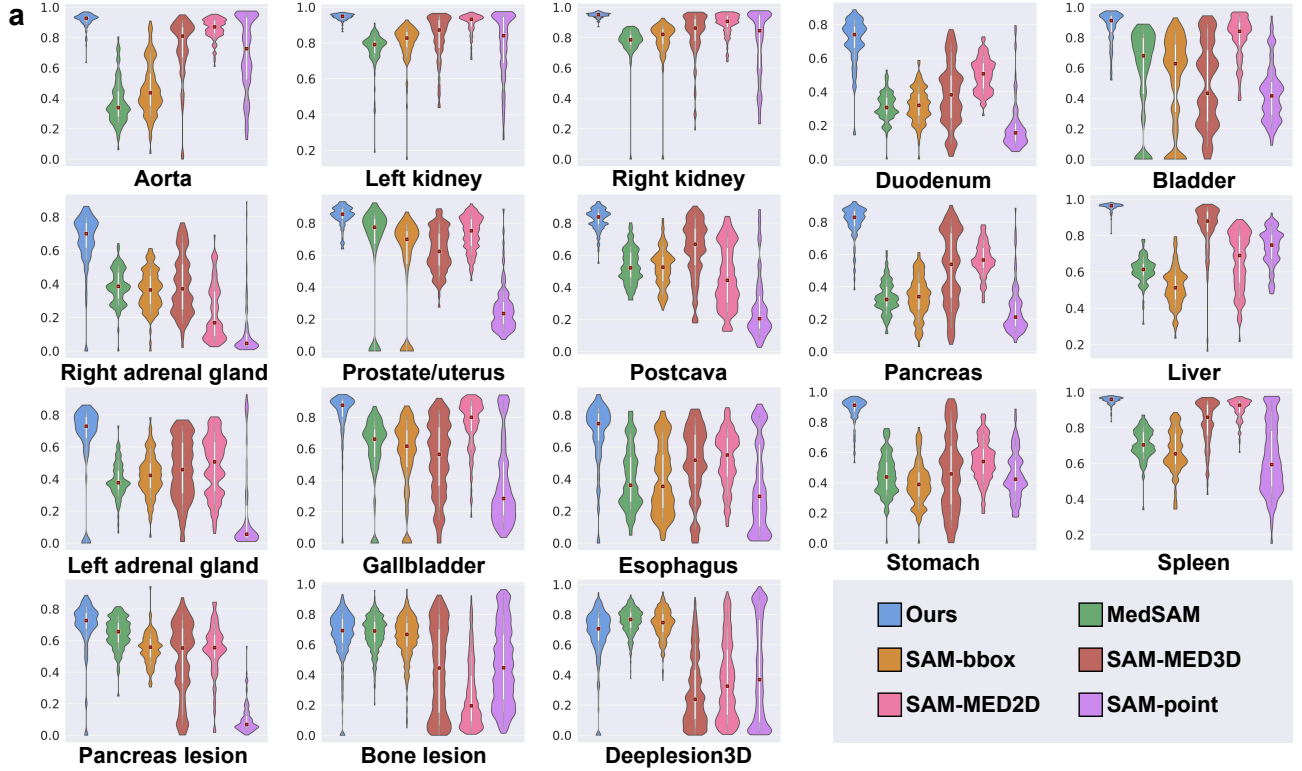


Figure 3. **Quantitative results of external validation experiments.** **a.** Violin plots for comparison experiment results of SegVol and interactive methods. The vertical axis represents the Dice score. **b.** The bar chart illustrates the consistency of SegVol’s performance on the external validation set across different prompt types.

Alexander Kirillov, et al. [31] discuss the multiple plausible outputs problem in the spatial prompt setting. As illustrated in the images on the top left in Fig. 5 b, they are applied with the same point prompt which reasonably corresponds to three concepts, namely, kidney tumor, left kidney, and the whole kidney. Similarly, in the bottom left images, the bounding box selects the region of liver. However, liver tumors, hepatic vessels, and liver itself are also plausible target structures. In these cases, SAM chooses to return multiple masks to match different levels of plausible results. Un-

like SAM’s solution, we use semantic prompts to clarify the targets. As shown in Fig. 5 b, the captions below the images are text prompts, and the masks in the images are the predictions of SegVol, which shows that the semantic prompts can effectively disambiguate the text prompts.

Furthermore, we study the possibility of SegVol to reflect spatial prompts to semantic categories. Fig. 5 c reveals that SegVol can give accurate semantic categories based on the spatial prompts. In the top left image in Fig. 5 c, the spatial prompt on the liver results in a 0.997 prediction score for

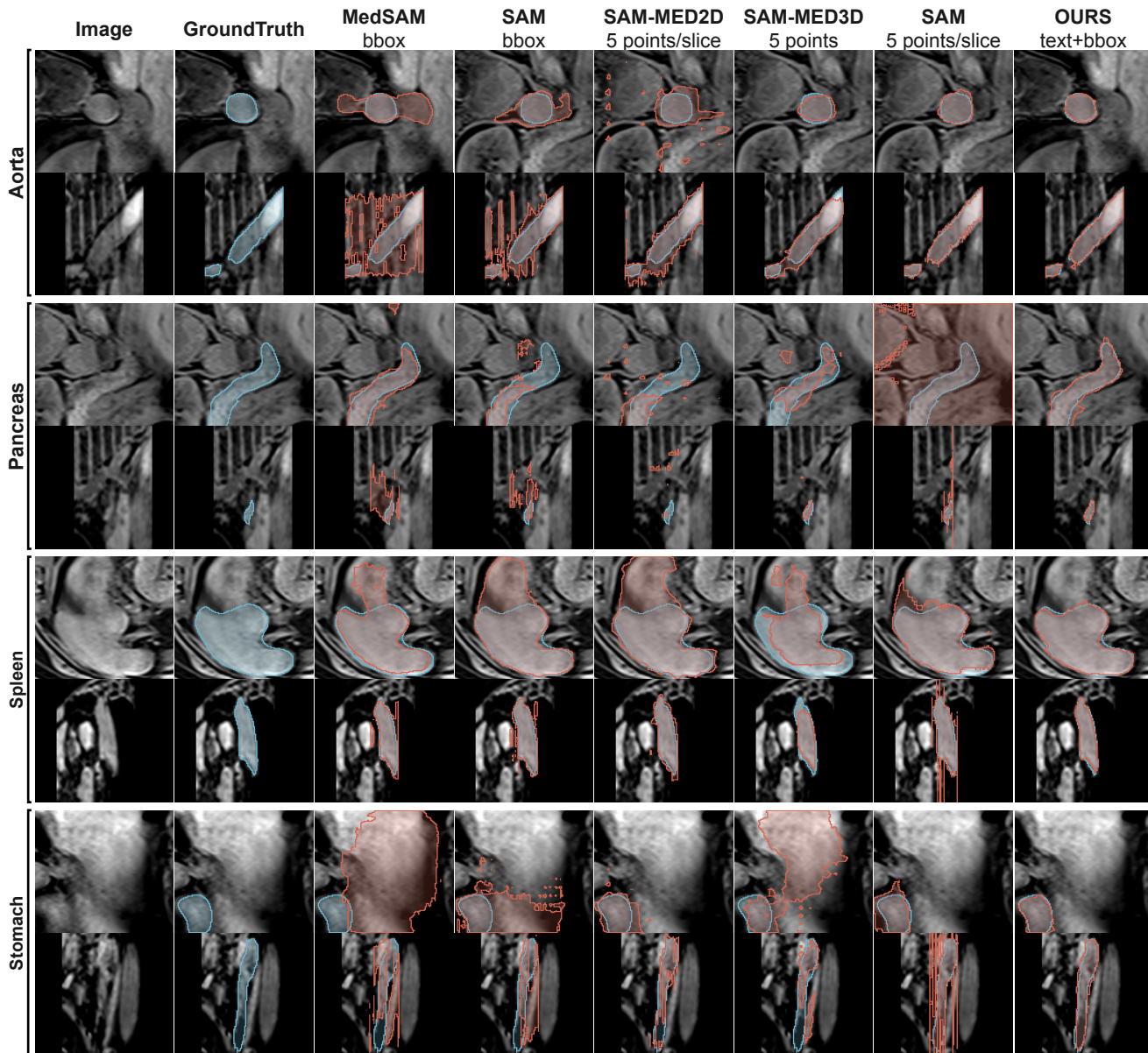


Figure 4. **Visualized prediction results of SegVol and other interactive methods on four external categories.** In each case, the upper row is the axial plane of CTs and the lower row is the sagittal plane of CTs. Visualization results show the accuracy and robustness of SegVol’s modeling of various anatomical structures.

liver. The top right image in the sub-figure shows if the spatial prompt is the point on the liver tumor, SegVol will output a 0.619 prediction score for tumor category and a 0.339 prediction score for liver based on the spatial relationship of liver tumor and liver. We implement this reflection experiment by decoding the semantic prompts from a category set and applying the softmax function among the logits of semantic prompts on the predicted mask voxels to get the prediction probabilities of different categories.

2.5. Scaling up training data

The success of scaling up has been witnessed in multiple computer vision tasks [31,45]. We conduct an ablation study to investigate the importance of scaling up training images and masks. The BTCV dataset [32], which includes 13 main organs, is set as an anchor to evaluate the model trained separately on 1, 2, and 8 datasets for 500 epochs, as well as the final model trained on 25 datasets. The detailed results are shown in Fig. 2 b. As a lightweight model, the performance is weak when only one dataset is used. However, with the

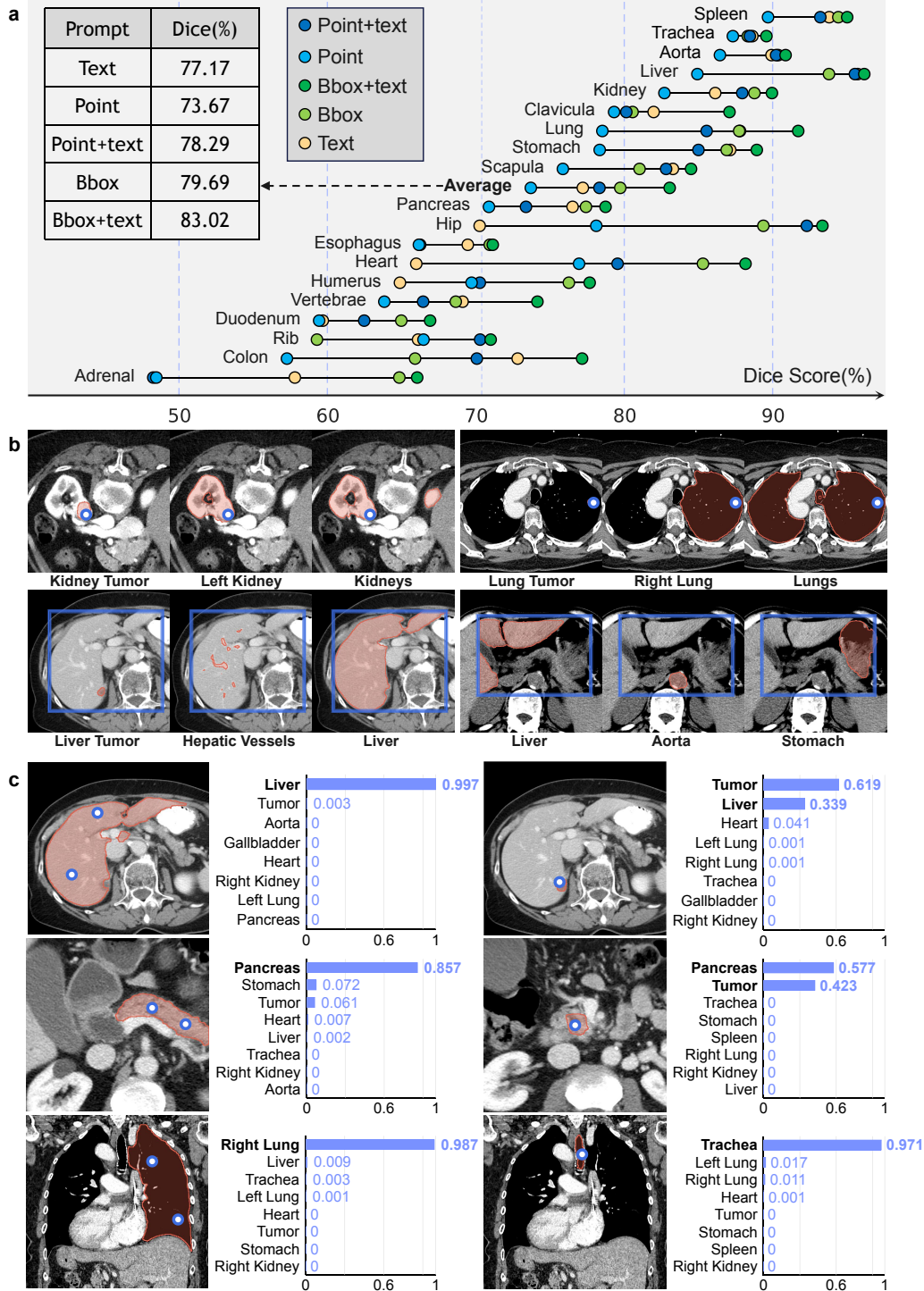


Figure 5. **Analysis of the relationship between semantic-prompt and spatial-prompt.** **a.** The quantitative experimental results on 19 internal tasks demonstrate that jointly using semantic and spatial prompts can achieve better performances. **b.** The four cases demonstrate that semantic prompts can clarify the ambiguity of spatial prompts and avoid multi-plausible outputs. Each image shows the segmentation result of SegVol using the spatial prompt, i.e. point or bounding box, and semantic prompt, i.e. the caption below the image. **c.** We reflect the spatial prompts to semantic categories (prompts). Each image shows the spatial prompt and the mask prediction. The bar charts rank the top 8 semantic categories with the highest probabilities.

increase of training data, the Dice score increases rapidly, especially in the text prompt setting. The results indicate that our method is scalable and better performance can be achieved if more training data is available.

3. Discussion

We present SegVol, a 3D foundational model for interactive and universal volumetric medical image segmentation. This method has been developed and evaluated using 25 open-source datasets, 10 internal validation tasks, and 18 external validation tasks. Unlike the traditional volumetric segmentation method, nnU-Net [24], which automatically configures settings for every dataset, SegVol is designed to unify various volumetric segmentation datasets into a single architecture. This results in a universal segmentation tool capable of generating accurate responses for over 200 anatomical targets. Furthermore, SegVol demonstrates state-of-the-art volumetric segmentation performance when compared with both traditional task-specific methods [15, 24, 33, 61] and the recent interactive methods [6, 31, 38, 64] in internal validation and external validation experiments, respectively. Despite its universality and high precision, SegVol maintains a lightweight architecture compared to other volumetric segmentation methods. We have made SegVol an open-source foundational model, readily applicable to a broad spectrum of medical image representation and analysis fields. This ensures it can be easily integrated and utilized by researchers and practitioners alike.

SegVol’s capability of interactive and precise segmentation makes it a promising clinical aid tool. It can assist clinicians in identifying and quantifying tumor location, size, and shape changes within a patient’s body [51] more accurately and rapidly. This precise monitoring aids clinicians in detecting tumor growth trends, assessing treatment effectiveness, and adjusting treatment plans as needed. Additionally, clinicians can use SegVol to accurately identify and segment important structures within a patient’s body, such as organs, blood vessels, or the precise location of tumors and surrounding tissues, using high-resolution 3D images such as CT volumes. These precise segmentation results help clinicians better understand the patient’s anatomical structures, plan surgical pathways, reduce surgical risks, and improve the accuracy and success rate of surgeries [41].

While SegVol is capable of understanding semantic prompts composed of sentences, there remains a gap between it and the referring expression segmentation that involves complex semantic information and logical relationships. The establishment of a referring expression segmentation model needs more curated data with spatial annotations with text. Our SegVol provides a foundation for realizing referring segmentation of medical images, and we leave as future work.

We primarily use SegVol with Computed Tomography (CT) data due to its advantages of easy acquisition, wide us-

age, and high resolution. CT is also the preferred method for evaluating solid tumors. Furthermore, the flexible architecture of SegVol allows it to be compatible with various types of volumetric medical images, like MRI. The current framework also allows for the direct addition of new training data in the same format, even if the new data are from unseen categories. This means that the model can inherit all previous knowledge and continue learning in new fields. This adaptability and continuous learning capabilities make SegVol a promising and broadly used tool in the field of medical image analysis.

4. Method

4.1. Data processing

One of the main challenges in volumetric medical image segmentation is the absence of large-scale publicly available volumetric medical data, especially the annotated segmentation CTs. Doing our utmost, we collected 25 open-source segmentation CT datasets, including CHAOS [28–30], HaN-Seg [44], AMOS22 [26], AbdomenCT-1k [39], KiTS23 [22], KiPA22 [18, 19, 55, 56], KiTS19 [21], BTCV [32], Pancreas-CT [8, 49, 50], 3D-IRCADB [59], FLARE22 [40, 58], TotalSegmentator [65], CT-ORG [2, 8, 47, 48], VerSe19, VerSe20 [34, 36, 53], SLIVER07 [20], QUBIQ [1], six MSD datasets [58], LUNA16 [54], and WORD [37]. These CTs originate from various medical institutions, captured by different machines with varying parameter settings and scanning regions. These factors result in a wide data distribution, and thus significant challenges in data processing.

To standardize these datasets, we perform the following transformation on every CT scan. Firstly, we set a threshold based on the mean voxel value of each volume. Voxels with values that are above this threshold are retained. Then, we calculate the 99.95th and 0.05th percentiles of the remaining voxels and use them as the upper and lower bounds to clip the original voxels and obtain the foreground. Finally, we normalize the foreground voxels using the mean and standard deviation.

Volumetric segmentation datasets suffer from the notorious problem of partial labels. Most of the datasets have annotations of only a few segmentation targets, e.g., several organs. Therefore, the deep models may learn the spurious correlation between datasets and segmentation targets, and produce inferior results during the inference phase. To relieve this problem, we introduce the pseudo labels by utilizing the Felzenswalb-Huttenlocher (FH) [11] algorithm to generate pseudo masks for each CT scan.

The unsupervised segmentation algorithm FH [11] separates the spatial structures based on the gradient between adjacent voxels. However, pseudo masks derived by the FH algorithm contain substantial noise and numerous small masks, for example, the disconnection of a complete struc-

ture and the wrong connection of different structures. To improve the pseudo masks, we employ the following strategies: 1) The pseudo masks are replaced with ground truth masks when applicable. 2) We filter out tiny structures smaller than 1% of the whole volume. 3) Each mask is refined by dilation and erosion operations.

4.2. Model architecture

The volumetric medical image segmentation dataset $\mathcal{D} = \{(\mathbf{x}_i, \mathbf{y}_i)\}$ consists of many pairs of 3D images and mask labels. Each data pair has a 3D image datum $\mathbf{x}_i \in \mathcal{R}^{C \times D \times H \times W}$ and K mask labels $\mathbf{y}_i \in \{0, 1\}^{K \times D \times H \times W}$, corresponding to K target categories. The classic segmentation model [15, 16, 24, 33, 61, 71] $\mathcal{F}(*, \theta)$ learns to predict masks \mathbf{y}_i belonging to the K categories based on the volumetric input \mathbf{x}_i , i.e., $\mathbf{o}_i = \mathcal{F}(\mathbf{x}_i, \theta)$, where $\mathbf{o}_i \in \mathcal{R}^{K \times D \times H \times W}$. Therefore, the traditional models are not able to generalize to unseen categories.

Motivated by the recent advance in 2D nature image segmentation, Segment Anything (SAM) [31], we design a novel method for interactive and universal volumetric medical image segmentation, named, SegVol. We illustrate the model in Fig. 1 a. SegVol supports three types of prompts for interactive segmentation: ‘bbox’ prompt, $\mathbf{b} \in \mathcal{R}^6$ representing the coordinates of two diagonal vertices; ‘point’ prompt, including a set of (P) points $\mathbf{p} \in \mathcal{R}^{P \times 3}$; and ‘text’ prompt, such as ‘liver’ or ‘cervical spine C2’, which is tokenized to tensor \mathbf{t} . SegVol consists of four modules, namely, image encoder $\mathcal{F}_{\text{IE}}(*, \theta_{\text{IE}})$, text encoder $\mathcal{F}_{\text{TE}}(*, \theta_{\text{TE}})$, prompt encoder $\mathcal{F}_{\text{PE}}(*, \theta_{\text{PE}})$, and mask decoder $\mathcal{F}_{\text{MD}}(*, \theta_{\text{MD}})$. We introduce each module in the following.

We employ ViT (Vision Transformer) [10] as the image encoder, which exhibits remarkable advantages over convolutional models [17] when pre-trained on large-scale datasets. We first pre-train ViT using SimMIM algorithm [66] on the all collected 96K CTs, and then conduct further supervised fine-tuning on the 6K CTs with 150K labeled segmentation masks. The image encoder, denoted as $\mathcal{F}_{\text{IE}}(*, \theta_{\text{IE}})$, takes a volumetric image $\mathbf{x} \in \mathcal{R}^{C \times D \times H \times W}$ as input. Firstly, it splits \mathbf{x} into a set of patches, denoted as $\mathbf{x}_{\text{patch}} \in \mathcal{R}^{N \times (C \times P_D \times P_H \times P_W)}$, where $N = \frac{D \times H \times W}{P_D \times P_H \times P_W}$. P_D , P_H and P_W are the size of patch. These patches are then fed into the network, which outputs an embedding $\mathbf{z}_{\text{image}} = \mathcal{F}_{\text{IE}}(\mathbf{x}_{\text{patch}}, \theta_{\text{IE}})$, $\mathbf{z}_{\text{image}} \in \mathcal{R}^{N \times F}$. F represents the feature dimension, which is set to 768 by default in this paper.

One main limitation of traditional segmentation models is that the models learn dataset-specific labels encoded as integers which cannot be generalized to new datasets or tasks, limiting their real-world applications. We enable universal segmentation across datasets by leveraging the text prompt. We employ the text encoder from CLIP model [45] to encode the input text prompt, as CLIP [45] has been trained

to align image and text on web-scale image-text pairs. We denote the text prompt encoder as $\mathcal{F}_{\text{TE}}(*, \theta_{\text{TE}})$. Given a word or phrase as prompt, we complete it using the template $s = \text{‘A computerized tomography of a [text prompt]’}$ [35]. s is then tokenized into \mathbf{t} . The text encoder accepts \mathbf{t} as input and outputs the text embedding $\mathbf{z}_{\text{text}} = \mathcal{F}_{\text{TE}}(\mathbf{t}, \theta_{\text{TE}})$, where $\mathbf{z}_{\text{text}} \in \mathcal{R}^F$. We freeze the off-the-shelf text encoder during training since the text data in CT datasets is a small amount.

Following SAM [31], we use the positional encoding [60] for point prompt \mathbf{p} and bbox prompt \mathbf{b} and obtain the point embedding $\mathbf{z}_{\text{point}} \in \mathcal{R}^F$ and bbox embedding $\mathbf{z}_{\text{bbox}} \in \mathcal{R}^F$. We concatenate the embeddings of three kinds of prompts as $\mathbf{z}_{\text{prompt}} = \mathcal{F}_{\text{PE}}(\mathbf{p}, \mathbf{b}, \mathbf{s}, \theta_{\text{PE}}) = [\mathbf{z}_{\text{point}}, \mathbf{z}_{\text{bbox}}, \mathbf{z}_{\text{text}}]$.

After obtaining the image embedding $\mathbf{z}_{\text{image}}$, prompt embedding $\mathbf{z}_{\text{prompt}}$ and text embedding \mathbf{z}_{text} , we input them to the mask decoder and predict the mask $\mathbf{p} = \mathcal{F}_{\text{MD}}(\mathbf{z}_{\text{image}}, \mathbf{z}_{\text{prompt}}, \mathbf{z}_{\text{text}}, \theta_{\text{MD}})$. We use self-attention and cross-attention [63] in two directions to blend the image embedding and prompt embedding, and then employ the transposed convolutions and interpolation operations to generate masks. Since the text embedding is the key to universal segmentation and it is also harder to learn the correlation between text and volumetric regions, we reinforce the text information by introducing a parallel text input \mathbf{z}_{text} beside the joint prompt embedding $\mathbf{z}_{\text{prompt}}$. We further compute a similarity matrix between the up-scaled embedding from the transposed convolution output and the text embedding in the mask decoder. The element-wise multiplication of the similarity matrix with the mask prediction is applied before interpolation, after which the model outputs the masks.

4.3. Prompt generation

SegVol can accept multiple prompt types, including individual point prompts, bbox prompts, and text prompts, and also their combinations. To make full use of the segmentation training data, we generate kinds of prompts for each datum. Then, the prompt and mask pairs are used to compute the training loss. SegVol supports ‘point’ prompts, ‘bbox’ prompts, and ‘text’ prompts.

The point prompt is built from ground truth or pseudo masks, consisting of three kinds of points, namely, positive point, negative point, and ignore point. Positive point means that it is within the target mask region, while negative points are those outside. The ignore points are used for input completion, which will be disregarded by the model so that the point prompt has the same length.

The bbox prompt is generated based on the ground truth or pseudo masks, integrated with random jitter to enhance the model’s robustness. When generating the bbox prompt for some pseudo mask, the bbox may also cover other masks due to the irregular 3D shapes. To address this problem, we compute the Intersection over Union (IOU) between the generated bbox and the included pseudo masks. Any mask with an IOU greater than 0.9 will also be integrated and con-

sidered as part of the target mask corresponding to this bbox prompt.

The bbox and point prompts can be generated by sampling points based on the ground-truth segmentation masks, while text prompts are constructed based on their category names. As pseudo masks produced by the unsupervised FH algorithm [11] do not have the semantic information, we only use point and bbox prompts when training with pseudo masks.

4.4. Loss function

We apply SimMIM algorithm [66] to pre-train the image encoder of SegVol using the masked image modeling loss $\mathcal{L}_{\text{pre-training}}(\theta_{\text{IE}}; \mathcal{D}_1)$. The loss function is as follows:

$$\mathcal{L}_{\text{pre-training}}(\theta_{\text{IE}}; \mathcal{D}_1) = \frac{1}{\Omega(\mathbf{x}_M)} \|\mathbf{y}_M - \mathbf{x}_M\|_1, \quad (1)$$

where $\mathbf{x}, \mathbf{y} \in \mathbb{R}^{D \times H \times W}$ are the input voxel values and predicted values, respectively. M denotes the set of masked voxels, $\Omega(\cdot)$ is the number of elements, and \mathcal{D}_1 is the pre-training dataset.

We combine the binary cross-entropy (BCE) loss and Dice loss as the supervised fine-tuning loss function $\mathcal{L}_{\text{fine-tuning}}(\theta; \mathcal{D}_2)$ to train the model with parameters θ , where $\theta = [\theta_{\text{IE}}, \theta_{\text{PE}}, \theta_{\text{MD}}]$ and \mathcal{D}_2 is the supervised fine-tuning dataset. The loss function is as follows:

$$\mathcal{L}_{\text{BCE}}(\theta; \mathcal{D}_2) = -\mathbb{E}_{(\mathbf{x}, \mathbf{y}) \sim \mathcal{D}_2} [\langle \mathbf{y}, \log(\mathcal{F}(\mathbf{x}, \theta)) \rangle + \langle 1 - \mathbf{y}, \log(1 - \mathcal{F}(\mathbf{x}, \theta)) \rangle] \quad (2)$$

$$\mathcal{L}_{\text{Dice}}(\theta; \mathcal{D}_2) = 1 - \mathbb{E}_{(\mathbf{x}, \mathbf{y}) \sim \mathcal{D}_2} \left[\frac{2\langle \mathbf{y}, \mathcal{F}(\mathbf{x}, \theta) \rangle}{\|\mathbf{y}\|_1 + \|\mathcal{F}(\mathbf{x}, \theta)\|_1} \right] \quad (3)$$

$$\mathcal{L}_{\text{fine-tuning}}(\theta; \mathcal{D}_2) = \mathcal{L}_{\text{BCE}}(\theta; \mathcal{D}_2) + \mathcal{L}_{\text{Dice}}(\theta; \mathcal{D}_2) \quad (4)$$

The detailed supervised fine-tuning training loop of SegVol is presented in Supplementary Algorithm 1.

4.5. Zoom-out-zoom-in mechanism

Compared to 2D slides, volumetric data has a remarkably large number of voxels meanwhile small segmentation targets relatively. Naively down-sampling the original data will cause serious information loss and thus inferior performance. Diving the large volumetric data into small cubes and conquering each separately is computationally expensive and also suffers from information loss. To reduce the computational cost while preserving the details of the Region of Interest (ROI), we design the zoom-out-zoom-in mechanism consisting of multi-size training and zoom-out-zoom-in inference.

To adapt various sizes of volumetric data and enable the zoom-out-zoom-in inference, we construct two kinds of training data. One is to resize the large-size CT to adapt the model’s input size and obtain the training data of the zoom-out view. The other one is to crop the original large-size CT into cubes with the model’s input size. In this way, we obtain the training data of zoom-in view.

During the zoom-out-zoom-in inference, we first zoom out and implement global inference. Given a large volumetric image, it is resized and then fed into the SegVol model. After obtaining the global predicted segmentation mask based on the user’s prompt, we locate the region of interest (ROI) and zoom in, namely, crop it from the original-size image. We apply a sliding window on the cropped region and implement more precise local inference. We adapt the input prompt for the local inference, since the original point and bbox prompts input by the user may not be applicable in the local inference region when zoom-in. Specifically, we ignore the positive or negative points of the local region. Similar to the training bbox prompt generation in Sec. 4.3, we generate the local bbox prompt by considering the global predicted mask in the local region as the pseudo mask. Finally, we fill the ROI region of the global segmentation mask with the local segmentation mask. The zoom-out-zoom-in mechanism realizes both efficient and precise inference simultaneously. The detailed procedure of zoom-out-zoom-in mechanism is provided in Supplementary Fig. 1 c and d.

4.6. Evaluation metrics

During the training and internal validation process, each subset of the joint dataset is divided into 80% training data and 20% internal validation data. To ensure the absence of any data leaks, hash value is utilized to compare between the validation set and the training set. And during the external validation process, the model’s parameters are all frozen.

We use the Dice Similarity Coefficient (Dice score) as a metric to evaluate the model, which is defined as $DSC = \frac{2|X \cap Y|}{|X| + |Y|}$. $|X \cap Y|$ is the cardinality of the intersection of the predicted segmentation sets X and the ground truth sets Y . $|X|$ and $|Y|$ are the cardinalities of sets X and Y respectively. Dice score is a commonly used metric for evaluating image segmentation tasks. It measures the degree of similarity between predicted segmentation and true segmentation, making it particularly suitable for evaluating the overlap degree of binary segmentation results.

5. Data and code availability

The training, internal, and external validation datasets used in this study are publicly accessible and licensed. Please refer to their original papers for the details of these datasets. The download links are provided in Supplementary Table 2.

Our training code, inference code, and model weights have been publicly available in <https://github.com/BAAI-DCAI/SegVol>. The online running demonstration is provided in <https://huggingface.co/spaces/BAAI/SegVol>.

Acknowledgement

Funding: This work is funded by the National Key R&D Program of China (2021ZD0111102) and NSFC-62306046.

References

- [1] Quantification of uncertainties in biomedical image quantification challenge 2021. <https://qubiq21.grand-challenge.org/>. Accessed: 18 Aug 2023.
- [2] Patrick Bilic, Patrick Christ, Hongwei Bran Li, Eugene Vorontsov, Avi Ben-Cohen, Georgios Kaissis, Adi Szeskin, Colin Jacobs, Gabriel Efrain Humpire Mamani, Gabriel Chartrand, et al. The liver tumor segmentation benchmark (lits). *Medical Image Analysis*, 84:102680, 2023.
- [3] brgfx. Image by brgfx on freepik. <https://www.freepik.com/free-vector/anatomical-structure-human-body/27539420.htm>.
- [4] Chen Chen, Chen Qin, Huaqi Qiu, Giacomo Tarroni, Jinming Duan, Wenjia Bai, and Daniel Rueckert. Deep learning for cardiac image segmentation: a review. *Frontiers in Cardiovascular Medicine*, 7:25, 2020.
- [5] Liang-Chieh Chen, George Papandreou, Iasonas Kokkinos, Kevin Murphy, and Alan L Yuille. Deeplab: Semantic image segmentation with deep convolutional nets, atrous convolution, and fully connected crfs. *IEEE transactions on pattern analysis and machine intelligence*, 40(4):834–848, 2017.
- [6] Junlong Cheng, Jin Ye, Zhongying Deng, Jianpin Chen, Tianbin Li, Haoyu Wang, Yanzhou Su, Ziyang Huang, Jilong Chen, Lei Jiang, et al. Sam-med2d. *arXiv preprint arXiv:2308.16184*, 2023.
- [7] Patrick Ferdinand Christ, Florian Ettliger, Felix Grün, Mohamed Ezzeldin A Elshaera, Jana Lipkova, Sebastian Schlecht, Freba Ahmaddy, Sunil Tatavarty, Marc Bickel, Patrick Bilic, et al. Automatic liver and tumor segmentation of ct and mri volumes using cascaded fully convolutional neural networks. *arXiv preprint arXiv:1702.05970*, 2017.
- [8] Kenneth Clark, Bruce Vendt, Kirk Smith, John Freymann, Justin Kirby, Paul Koppel, Stephen Moore, Stanley Phillips, David Maffitt, Michael Pringle, et al. The cancer imaging archive (tcia): maintaining and operating a public information repository. *Journal of digital imaging*, 26:1045–1057, 2013.
- [9] Max de Grauw. Universal lesion segmentation challenge 23. <https://uls23.grand-challenge.org/>.
- [10] Alexey Dosovitskiy, Lucas Beyer, Alexander Kolesnikov, Dirk Weissenborn, Xiaohua Zhai, Thomas Unterthiner, Mostafa Dehghani, Matthias Minderer, Georg Heigold, Sylvain Gelly, Jakob Uszkoreit, and Neil Houlsby. An image is worth 16x16 words: Transformers for image recognition at scale, 2021.
- [11] Pedro F Felzenszwalb and Daniel P Huttenlocher. Efficient graph-based image segmentation. *International journal of computer vision*, 59:167–181, 2004.
- [12] Vincenzo Ferrari, Marina Carbone, Carla Cappelli, Luigi Boni, Franca Melfi, Mauro Ferrari, Franco Mosca, and Andrea Pietrabissa. Value of multidetector computed tomography image segmentation for preoperative planning in general surgery. *Surgical endoscopy*, 26:616–626, 2012.
- [13] Zaiwang Gu, Jun Cheng, Huazhu Fu, Kang Zhou, Huaying Hao, Yitian Zhao, Tianyang Zhang, Shenghua Gao, and Jiang Liu. Ce-net: Context encoder network for 2d medical image segmentation. *IEEE transactions on medical imaging*, 38(10):2281–2292, 2019.
- [14] A Ben Hamida, Maxime Devanne, Jonathan Weber, Caroline Truntzer, Valentin Derangère, François Ghiringhelli, Germain Forestier, and Cédric Wemmert. Deep learning for colon cancer histopathological images analysis. *Computers in Biology and Medicine*, 136:104730, 2021.
- [15] Ali Hatamizadeh, Vishwesh Nath, Yucheng Tang, Dong Yang, Holger Roth, and Daguang Xu. Swin unetr: Swin transformers for semantic segmentation of brain tumors in mri images, 2022.
- [16] Ali Hatamizadeh, Yucheng Tang, Vishwesh Nath, Dong Yang, Andriy Myronenko, Bennett Landman, Holger R Roth, and Daguang Xu. Unetr: Transformers for 3d medical image segmentation. In *Proceedings of the IEEE/CVF winter conference on applications of computer vision*, pages 574–584, 2022.
- [17] Kaiming He, Xiangyu Zhang, Shaoqing Ren, and Jian Sun. Deep residual learning for image recognition. In *Proceedings of the IEEE conference on computer vision and pattern recognition*, pages 770–778, 2016.
- [18] Yuting He, Guanyu Yang, Jian Yang, Yang Chen, Youyong Kong, Jiasong Wu, Lijun Tang, Xiaomei Zhu, Jean-Louis Dillenseger, Pengfei Shao, et al. Dense biased networks with deep priori anatomy and hard region adaptation: Semi-supervised learning for fine renal artery segmentation. *Medical image analysis*, 63:101722, 2020.
- [19] Yuting He, Guanyu Yang, Jian Yang, Rongjun Ge, Youyong Kong, Xiaomei Zhu, Shaobo Zhang, Pengfei Shao, Huazhong Shu, Jean-Louis Dillenseger, et al. Meta grayscale adaptive network for 3d integrated renal structures segmentation. *Medical image analysis*, 71:102055, 2021.
- [20] Tobias Heimann, Bram Van Ginneken, Martin A Styner, Yulia Arzhaeva, Volker Aurich, Christian Bauer, Andreas Beck, Christoph Becker, Reinhard Beichel, György Bekes, et al. Comparison and evaluation of methods for liver segmentation from ct datasets. *IEEE transactions on medical imaging*, 28(8):1251–1265, 2009.
- [21] Nicholas Heller, Fabian Isensee, Klaus H Maier-Hein, Xiaoshuai Hou, Chunmei Xie, Fengyi Li, Yang Nan, Guangrui Mu, Zhiyong Lin, Miofei Han, et al. The state of the art in kidney and kidney tumor segmentation in contrast-enhanced ct imaging: Results of the kits19 challenge. *Medical Image Analysis*, page 101821, 2020.
- [22] Nicholas Heller, Fabian Isensee, Dasha Trofimova, Resha Tejjapaul, Zhongchen Zhao, Huai Chen, Lisheng Wang, Alex Golts, Daniel Khapun, Daniel Shats, Yoel Shoshan, Flora Gilboa-Solomon, Yasmeen George, Xi Yang, Jianpeng Zhang, Jing Zhang, Yong Xia, Mengran Wu, Zhiyang Liu, Ed Walczak, Sean McSweeney, Ranveer Vasdev, Chris Hornung, Rafat Solaiman, Jamee Schoephoerster, Bailey Abernathy,

- David Wu, Safa Abdulkadir, Ben Byun, Justice Spriggs, Griffin Struyk, Alexandra Austin, Ben Simpson, Michael Hagstrom, Sierra Virnig, John French, Nitin Venkatesh, Sarah Chan, Keenan Moore, Anna Jacobsen, Susan Austin, Mark Austin, Subodh Regmi, Nikolaos Papanikolopoulos, and Christopher Weight. The kits21 challenge: Automatic segmentation of kidneys, renal tumors, and renal cysts in corticomedullary-phase ct, 2023.
- [23] Tianrui Hui, Si Liu, Shaofei Huang, Guanbin Li, Sansi Yu, Faxi Zhang, and Jizhong Han. Linguistic structure guided context modeling for referring image segmentation. In *Computer Vision—ECCV 2020: 16th European Conference, Glasgow, UK, August 23–28, 2020, Proceedings, Part X 16*, pages 59–75. Springer, 2020.
- [24] Fabian Isensee, Paul F Jaeger, Simon AA Kohl, Jens Petersen, and Klaus H Maier-Hein. nnu-net: a self-configuring method for deep learning-based biomedical image segmentation. *Nature methods*, 18(2):203–211, 2021.
- [25] Debesh Jha, Michael A Riegler, Dag Johansen, Pål Halvorsen, and Håvard D Johansen. Doubleu-net: A deep convolutional neural network for medical image segmentation. In *2020 IEEE 33rd International Symposium on Computer-Based Medical Systems (CBMS)*, pages 558–564. IEEE, 2020.
- [26] Yuanfeng Ji, Haotian Bai, Jie Yang, Chongjian Ge, Ye Zhu, Ruimao Zhang, Zhen Li, Lingyan Zhang, Wanling Ma, Xiang Wan, et al. Amos: A large-scale abdominal multi-organ benchmark for versatile medical image segmentation. *arXiv preprint arXiv:2206.08023*, 2022.
- [27] Huiyan Jiang, Zhaoshuo Diao, and Yu-Dong Yao. Deep learning techniques for tumor segmentation: a review. *The Journal of Supercomputing*, 78(2):1807–1851, 2022.
- [28] A. Emre Kavur, N. Sinem Gezer, Mustafa Bar, Sinem Aslan, Pierre-Henri Conze, Vladimir Groza, Duc Duy Pham, Soumick Chatterjee, Philipp Ernst, Sava zkan, Bora Baydar, Dmitry Lachinov, Shuo Han, Josef Pauli, Fabian Isensee, Matthias Perkonigg, Rachana Sathish, Ronnie Rajan, Debodoot Sheet, Gurbandurdy Dovletov, Oliver Speck, Andreas Nrnberger, Klaus H. Maier-Hein, Gzde Bozda Akar, Gzde nal, Ouz Dicle, and M. Alper Selver. Chaos challenge - combined (ct-mr) healthy abdominal organ segmentation. *Medical Image Analysis*, 69:101950, Apr. 2021.
- [29] A. Emre Kavur, Naciye Sinem Gezer, Mustafa Bar, Yusuf ahin, Sava zkan, Bora Baydar, Ula Yksel, alar Klker, ahin Olut, Gzde Bozda Akar, Gzde nal, Ouz Dicle, and M. Alper Selver. Comparison of semi-automatic and deep learning based automatic methods for liver segmentation in living liver transplant donors. *Diagnostic and Interventional Radiology*, 26:11–21, Jan. 2020.
- [30] Ali Emre Kavur, M. Alper Selver, Ouz Dicle, Mustafa Bar, and N. Sinem Gezer. Chaos - combined (ct-mr) healthy abdominal organ segmentation challenge data. Apr. 2019.
- [31] Alexander Kirillov, Eric Mintun, Nikhila Ravi, Hanzi Mao, Chloe Rolland, Laura Gustafson, Tete Xiao, Spencer Whitehead, Alexander C Berg, Wan-Yen Lo, et al. Segment anything. *arXiv preprint arXiv:2304.02643*, 2023.
- [32] Bennett Landman, Zhoubing Xu, J Igelsias, Martin Styner, T Langerak, and Arno Klein. Miccai multi-atlas labeling beyond the cranial vault-workshop and challenge. In *Proc. MICCAI Multi-Atlas Labeling Beyond Cranial Vault Workshop Challenge*, volume 5, page 12, 2015.
- [33] Ho Hin Lee, Shunxing Bao, Yuankai Huo, and Bennett A. Landman. 3d ux-net: A large kernel volumetric convnet modernizing hierarchical transformer for medical image segmentation, 2023.
- [34] Hans Liebl, David Schinz, Anjany Sekuboyina, Luca Malagutti, Maximilian T Löffler, Amirhossein Bayat, Malek El Husseini, Giles Tetteh, Katharina Grau, Eva Niederreiter, et al. A computed tomography vertebral segmentation dataset with anatomical variations and multi-vendor scanner data. *Scientific data*, 8(1):284, 2021.
- [35] Jie Liu, Yixiao Zhang, Jie-Neng Chen, Junfei Xiao, Yongyi Lu, Bennett A. Landman, Yixuan Yuan, Alan Yuille, Yucheng Tang, and Zongwei Zhou. Clip-driven universal model for organ segmentation and tumor detection, 2023.
- [36] Maximilian T Löffler, Anjany Sekuboyina, Alina Jacob, Anna-Lena Grau, Andreas Scharr, Malek El Husseini, Mareike Kallweit, Claus Zimmer, Thomas Baum, and Jan S Kirschke. A vertebral segmentation dataset with fracture grading. *Radiology: Artificial Intelligence*, 2(4):e190138, 2020.
- [37] Xiangde Luo, Wenjun Liao, Jianghong Xiao, Jieneng Chen, Tao Song, Xiaofan Zhang, Kang Li, Dimitris N. Metaxas, Guotai Wang, and Shaoting Zhang. WORD: A large scale dataset, benchmark and clinical applicable study for abdominal organ segmentation from ct image. *Medical Image Analysis*, 82:102642, 2022.
- [38] Jun Ma, Yuting He, Feifei Li, Lin Han, Chenyu You, and Bo Wang. Segment anything in medical images, 2023.
- [39] Jun Ma, Yao Zhang, Song Gu, Cheng Zhu, Cheng Ge, Yichi Zhang, Xingle An, Congcong Wang, Qiyuan Wang, Xin Liu, Shucheng Cao, Qi Zhang, Shangqing Liu, Yunpeng Wang, Yuhui Li, Jian He, and Xiaoping Yang. Abdomenct-1k: Is abdominal organ segmentation a solved problem? *IEEE Transactions on Pattern Analysis and Machine Intelligence*, 44(10):6695–6714, 2022.
- [40] Jun Ma, Yao Zhang, Song Gu, Cheng Zhu, Cheng Ge, Yichi Zhang, Xingle An, Congcong Wang, Qiyuan Wang, Xin Liu, et al. Abdomenct-1k: Is abdominal organ segmentation a solved problem? *IEEE Transactions on Pattern Analysis and Machine Intelligence*, 44(10):6695–6714, 2021.
- [41] Jordi Minnema, Anne Ernst, Maureen van Eijnatten, Ruben Pauwels, Tymour Forouzanfar, Kees Joost Batenburg, and Jan Wolff. A review on the application of deep learning for ct reconstruction, bone segmentation and surgical planning in oral and maxillofacial surgery. *Dentomaxillofacial Radiology*, 51(7):20210437, 2022.
- [42] Mehreen Mubashar, Hazrat Ali, Christer Grönlund, and Shoaib Azmat. R2u++: a multiscale recurrent residual u-net with dense skip connections for medical image segmentation. *Neural Computing and Applications*, 34(20):17723–17739, 2022.
- [43] Ishak Pacal, Dervis Karaboga, Alper Basturk, Bahriye Akay, and Ufuk Nalbantoglu. A comprehensive review of deep learning in colon cancer. *Computers in Biology and Medicine*, 126:104003, 2020.
- [44] Gašper Podobnik, Primož Strojjan, Primož Peterlin, Bulat Ibragimov, and Tomaž Vrtovec. Han-seg: The head and

- neck organ-at-risk ct and mr segmentation dataset. *Medical physics*, 50(3):1917–1927, 2023.
- [45] Alec Radford, Jong Wook Kim, Chris Hallacy, Aditya Ramesh, Gabriel Goh, Sandhini Agarwal, Girish Sastry, Amanda Askell, Pamela Mishkin, Jack Clark, et al. Learning transferable visual models from natural language supervision. In *International conference on machine learning*, pages 8748–8763. PMLR, 2021.
- [46] Hiba Ramadan, Chaymae Lachqar, and Hamid Tairi. A survey of recent interactive image segmentation methods. *Computational visual media*, 6:355–384, 2020.
- [47] Blaine Rister, Kaushik Shivakumar, Tomomi Nobashi, and Daniel L Rubin. Ct-org: Ct volumes with multiple organ segmentations [dataset]. *The Cancer Imaging Archive*, 2019.
- [48] Blaine Rister, Darvin Yi, Kaushik Shivakumar, Tomomi Nobashi, and Daniel L Rubin. Ct organ segmentation using gpu data augmentation, unsupervised labels and iou loss. *arXiv preprint arXiv:1811.11226*, 2018.
- [49] Holger R Roth, Amal Farag, E Turkbey, Le Lu, Jiamin Liu, and Ronald M Summers. Data from pancreas-ct. the cancer imaging archive. *IEEE Transactions on Image Processing*, 2016.
- [50] Holger R Roth, Le Lu, Amal Farag, Hoo-Chang Shin, Jiamin Liu, Evrim B Turkbey, and Ronald M Summers. Deeporgan: Multi-level deep convolutional networks for automated pancreas segmentation. In *Medical Image Computing and Computer-Assisted Intervention–MICCAI 2015: 18th International Conference, Munich, Germany, October 5-9, 2015, Proceedings, Part I 18*, pages 556–564. Springer, 2015.
- [51] Sidra Sajid, Saddam Hussain, and Amna Sarwar. Brain tumor detection and segmentation in mr images using deep learning. *Arabian Journal for Science and Engineering*, 44:9249–9261, 2019.
- [52] Gihan Samarasinghe, Michael Jameson, Shalini Vinod, Matthew Field, Jason Dowling, Arcot Sowmya, and Lois Holloway. Deep learning for segmentation in radiation therapy planning: a review. *Journal of Medical Imaging and Radiation Oncology*, 65(5):578–595, 2021.
- [53] Anjany Sekuboyina, Malek E Hussein, Amirhossein Bayat, Maximilian Löffler, Hans Liebl, Hongwei Li, Giles Tetteh, Jan Kukačka, Christian Payer, Darko Štern, et al. Verse: a vertebrae labelling and segmentation benchmark for multi-detector ct images. *Medical image analysis*, 73:102166, 2021.
- [54] Arnaud Arindra Adiyoso Setio, Alberto Traverso, Thomas De Bel, Moira SN Berens, Cas Van Den Bogaard, Piergiorgio Cerello, Hao Chen, Qi Dou, Maria Evelina Fantacci, Bram Geurts, et al. Validation, comparison, and combination of algorithms for automatic detection of pulmonary nodules in computed tomography images: the luna16 challenge. *Medical image analysis*, 42:1–13, 2017.
- [55] Pengfei Shao, Chao Qin, Changjun Yin, Xiaoxin Meng, Xiaobing Ju, Jie Li, Qiang Lv, Wei Zhang, and Zhengquan Xu. Laparoscopic partial nephrectomy with segmental renal artery clamping: technique and clinical outcomes. *European urology*, 59(5):849–855, 2011.
- [56] Pengfei Shao, Lijun Tang, Pu Li, Yi Xu, Chao Qin, Qiang Cao, Xiaobing Ju, Xiaoxin Meng, Qiang Lv, Jie Li, et al. Precise segmental renal artery clamping under the guidance of dual-source computed tomography angiography during laparoscopic partial nephrectomy. *European urology*, 62(6):1001–1008, 2012.
- [57] Nahian Siddique, Sidike Paheding, Colin P Elkin, and Vijay Devabhaktuni. U-net and its variants for medical image segmentation: A review of theory and applications. *Ieee Access*, 9:82031–82057, 2021.
- [58] Amber L Simpson, Michela Antonelli, Spyridon Bakas, Michel Bilello, Keyvan Farahani, Bram Van Ginneken, Annette Kopp-Schneider, Bennett A Landman, Geert Litjens, Bjoern Menze, et al. A large annotated medical image dataset for the development and evaluation of segmentation algorithms. *arXiv preprint arXiv:1902.09063*, 2019.
- [59] Luc Soler, Alexandre Hostettler, Vincent Agnus, Arnaud Charnoz, Jean-Baptiste Fasquel, Johan Moreau, Anne-Blandine Osswald, Mourad Bouhadjar, and Jacques Marescaux. 3d image reconstruction for comparison of algorithm database. URL: <https://www.ircad.fr/research/datasets/liver-segmentation-3d-ircadb-01>, 2010.
- [60] Matthew Tancik, Pratul P. Srinivasan, Ben Mildenhall, Sara Fridovich-Keil, Nithin Raghavan, Utkarsh Singhal, Ravi Ramamoorthi, Jonathan T. Barron, and Ren Ng. Fourier features let networks learn high frequency functions in low dimensional domains, 2020.
- [61] Yucheng Tang, Dong Yang, Wenqi Li, Holger R Roth, Bennett Landman, Daguang Xu, Vishwesh Nath, and Ali Hatamizadeh. Self-supervised pre-training of swin transformers for 3d medical image analysis. In *Proceedings of the IEEE/CVF Conference on Computer Vision and Pattern Recognition*, pages 20730–20740, 2022.
- [62] Stefano Trebeschi, Zuhir Bodalal, Thierry N Boellaard, Teresa M Tareco Bucho, Silvia G Drago, Ieva Kurilova, Adriana M Calin-Vainak, Andrea Delli Pizzi, Mirte Muller, Karlijn Hummelink, et al. Prognostic value of deep learning-mediated treatment monitoring in lung cancer patients receiving immunotherapy. *Frontiers in Oncology*, 11:609054, 2021.
- [63] Ashish Vaswani, Noam Shazeer, Niki Parmar, Jakob Uszkoreit, Llion Jones, Aidan N. Gomez, Lukasz Kaiser, and Illia Polosukhin. Attention is all you need, 2023.
- [64] Haoyu Wang, Sizheng Guo, Jin Ye, Zhongying Deng, Junlong Cheng, Tianbin Li, Jianpin Chen, Yanzhou Su, Ziyang Huang, Yiqing Shen, Bin Fu, Shaoting Zhang, Junjun He, and Yu Qiao. Sam-med3d, 2023.
- [65] J Wasserthal, M Meyer, HC Breit, J Cyriac, S Yang, and M Segeroth. Totalsegmentator: Robust segmentation of 104 anatomical structures in ct images 2022. *arXiv*, 2022.
- [66] Zhenda Xie, Zheng Zhang, Yue Cao, Yutong Lin, Jianmin Bao, Zhuliang Yao, Qi Dai, and Han Hu. Simmim: A simple framework for masked image modeling, 2022.
- [67] Xiao-Xia Yin, Le Sun, Yuhang Fu, Ruiliang Lu, Yanchun Zhang, et al. U-net-based medical image segmentation. *Journal of Healthcare Engineering*, 2022, 2022.
- [68] Habib Zaidi and Issam El Naqa. Pet-guided delineation of radiation therapy treatment volumes: a survey of image segmentation techniques. *European journal of nuclear medicine and molecular imaging*, 37:2165–2187, 2010.

- [69] Jiawei Zhang, Yuzhen Jin, Jilan Xu, Xiaowei Xu, and Yanchun Zhang. Mdu-net: Multi-scale densely connected u-net for biomedical image segmentation. *arXiv preprint arXiv:1812.00352*, 2018.
- [70] Ziang Zhang, Chengdong Wu, Sonya Coleman, and Dermot Kerr. Dense-inception u-net for medical image segmentation. *Computer methods and programs in biomedicine*, 192:105395, 2020.
- [71] Hong-Yu Zhou, Jiansen Guo, Yinghao Zhang, Lequan Yu, Liansheng Wang, and Yizhou Yu. nnformer: Interleaved transformer for volumetric segmentation, 2022.
- [72] Zongwei Zhou, Md Mahfuzur Rahman Siddiquee, Nima Tajbakhsh, and Jianming Liang. Unet++: A nested u-net architecture for medical image segmentation. In *Deep Learning in Medical Image Analysis and Multimodal Learning for Clinical Decision Support: 4th International Workshop, DLMIA 2018, and 8th International Workshop, ML-CDS 2018, Held in Conjunction with MICCAI 2018, Granada, Spain, September 20, 2018, Proceedings 4*, pages 3–11. Springer, 2018.

Supplementary Materials

Table 1. Supervised fine-tuning datasets and validation datasets.

Dataset	Anatomical Targets	Category Number	Trainset Volumes
3D-IRCADB [59]	Liver and liver tumor	47	20
AbdomenCT-1k [39]	Liver, kidney, spleen, and pancreas	4	1000
AMOS22 [26]	Abdominal organs	15	240
BTCV [32]	Abdominal organs	13	30
CHAOS [28–30]	Abdominal organs	1	20
CT-ORG [2, 8, 47, 48]	Brain, lung, bones, liver, kidney, and bladder	6	140
FLARE22 [40, 58]	Thoracic and abdominal organs	13	50
HaN-Seg [44]	Organs of the head and neck	30	42
KiPA22 [18, 19, 55, 56]	Kidney, renal tumor, artery, and vein	4	70
KiTS19 [21]	Kidney and kidney tumor	2	210
KiTS23 [22]	Kidney, kidney tumor, and kidney cyst	3	489
LUNA16 [54]	Left lung, right lung, and trachea	3	888
MSD-Colon [58]	Colon tumor	1	126
MSD-HepaticVessel [58]	Hepatic vessel and liver tumor	2	303
MSD-Liver [58]	Liver and liver tumor	2	131
MSD-lung [58]	Lung tumor	1	63
MSD-pancreas [58]	Pancreas and pancreas tumor	2	281
MSD-spleen [58]	Spleen	1	41
Pancreas-CT [8, 49, 50]	Pancreas	1	82
QUBIQ [1]	Kidney, pancreas, and pancreas lesion	3	82
SLIVER07 [20]	Liver	1	20
TotalSegmentator [65]	Organs of the whole body	104	1203
ULS23(novel annotated set) [9]	Various lesions	-	1618
VerSe19 [34, 36, 53]	Vertebrae	28	80
VerSe20 [34, 36, 53]	vertebrae	28	61
WORD [37]	Thoracic and abdominal organs	16	100

Table 2. Data availability for supervised fine-tuning datasets and validation datasets.

Dataset	Link
3D-IRCADB [59]	https://www.kaggle.com/datasets/nguyenhoainam27/3dircadb
AbdomenCT-1k [39]	https://github.com/JunMa11/AbdomenCT-1K
AMOS22 [26]	https://amos22.grand-challenge.org/
BTCV [32]	https://www.synapse.org/#!/Synapse:syn3193805/wiki/217752
CHAOS [28–30]	https://chaos.grand-challenge.org/
CT-ORG [2, 8, 47, 48]	https://wiki.cancerimagingarchive.net/pages/viewpage.action?pageId=61080890
FLARE22 [40, 58]	https://flare22.grand-challenge.org/
HaN-Seg [44]	https://han-seg2023.grand-challenge.org/
KiPA22 [18, 19, 55, 56]	https://kipa22.grand-challenge.org/
KiTS19 [21]	https://kits19.grand-challenge.org/
KiTS23 [22]	https://kits-challenge.org/kits23/
LUNA16 [54]	https://luna16.grand-challenge.org/Data/
MSD-Colon [58]	http://medicaldecathlon.com/
MSD-HepaticVessel [58]	http://medicaldecathlon.com/
MSD-Liver [58]	http://medicaldecathlon.com/
MSD-lung [58]	http://medicaldecathlon.com/
MSD-pancreas [58]	http://medicaldecathlon.com/
MSD-spleen [58]	http://medicaldecathlon.com/
Pancreas-CT [8, 49, 50]	https://wiki.cancerimagingarchive.net/display/public/pancreas-ct
QUBIQ [1]	https://qubiq.grand-challenge.org/
SLIVER07 [20]	https://sliver07.grand-challenge.org/
TotalSegmentator [65]	https://github.com/wasserth/TotalSegmentator
ULS23 [9]	https://uls23.grand-challenge.org/
VerSe19 [34, 36, 53]	https://osf.io/nqjyw/
VerSe20 [34, 36, 53]	https://osf.io/t98fz/
WORD [37]	https://paperswithcode.com/dataset/word

Table 3. Internal validation results of 3DUX-NET, SwinUNETR, nnU-Net and SegVol on the test set of supervised fine-tuning datasets in term of Dice score.

Category	3DUX-NET [33]	SwinUNETR [15]	nnU-Net [24]	SegVol
Aorta	0.9122 (0.8852, 0.9292)	0.8870 (0.8619, 0.8964)	0.9155 (0.8790, 0.9431)	0.9179 (0.8850, 0.9256)
Colon cancer	0.0773 (0.0000, 0.2931)	0.0270 (0.0003, 0.2908)	0.3610 (0.0000, 0.6961)	0.7582 (0.6749, 0.7903)
Esophagus	0.7136 (0.6617, 0.7718)	0.6063 (0.5508, 0.6353)	0.7407 (0.6563, 0.8313)	0.7373 (0.7205, 0.8062)
Gallbladder	0.4916 (0.1875, 0.6926)	0.2714 (0.1421, 0.5671)	0.8555 (0.5267, 0.8633)	0.8560 (0.7036, 0.8968)
Inferior vena cava	0.7673 (0.6740, 0.8465)	0.7368 (0.6376, 0.8376)	0.8138 (0.7580, 0.8487)	0.8267 (0.8044, 0.8418)
Left adrenal gland	0.5788 (0.3238, 0.6038)	0.5658 (0.4380, 0.6147)	0.7915 (0.6888, 0.8231)	0.7643 (0.6525, 0.7880)
Left kidney	0.9072 (0.8692, 0.9438)	0.9070 (0.8829, 0.9203)	0.9395 (0.9050, 0.9518)	0.9296 (0.9228, 0.9321)
Liver	0.9316 (0.9074, 0.9462)	0.9374 (0.9110, 0.9531)	0.9276 (0.8614, 0.9597)	0.9560 (0.9437, 0.9685)
Liver tumor	0.7131 (0.5159, 0.8457)	0.6479 (0.2756, 0.7853)	0.7495 (0.6243, 0.8228)	0.7801 (0.7558, 0.8440)
Lung tumor	0.5628 (0.4375, 0.7021)	0.4043 (0.2159, 0.6910)	0.7294 (0.4814, 0.8210)	0.7250 (0.6026, 0.8154)
Pancreas	0.5820 (0.4748, 0.7069)	0.6352 (0.5586, 0.6894)	0.8248 (0.8169, 0.8665)	0.8464 (0.8248, 0.8578)
Portal/splenic vein	0.7207 (0.6211, 0.7588)	0.6656 (0.5888, 0.6982)	0.7964 (0.7524, 0.8582)	0.7188 (0.7128, 0.7569)
Right adrenal gland	0.5785 (0.5099, 0.6302)	0.5026 (0.2730, 0.5963)	0.7137 (0.7067, 0.7326)	0.6579 (0.6372, 0.7008)
Right kidney	0.9177 (0.8877, 0.9417)	0.9065 (0.9011, 0.9289)	0.9432 (0.9207, 0.9504)	0.9227 (0.9157, 0.9295)
Spleen	0.8913 (0.7726, 0.9492)	0.9147 (0.8255, 0.9456)	0.9681 (0.9596, 0.9766)	0.9642 (0.9558, 0.9664)
Stomach	0.7627 (0.6655, 0.8424)	0.7147 (0.6470, 0.8231)	0.8374 (0.6339, 0.9391)	0.9177 (0.9035, 0.9260)

Table 4. Generalization experiment results of SegVol on the MRI set of CHAOS [28–30] dataset in term of Dice score.

Method	Liver	Spleen	Left Kidney	Right Kidney
SegVol(5 Points)	0.8091 (0.7376, 0.8554)	0.7496 (0.6990, 0.7872)	0.7216 (0.6125, 0.7869)	0.7174 (0.6052, 0.8090)
SegVol(Bbox)	0.8570 (0.8319, 0.8819)	0.8009 (0.7702, 0.8256)	0.8004 (0.7265, 0.8452)	0.8146 (0.7593, 0.8620)

Table 5. External validation results of SAM(Point), SAM(Bbox), SAM-MED2D, SAM-MED3D, MedSAM and SegVol on the external validation datasets in term of Dice score.

Category	SAM(Point) [31]	SAM(Bbox) [31]	SAM-MED2D [6]	SAM-MED3D [64]	MedSAM [38]	SegVol
Aorta	0.7267 (0.5213, 0.9350)	0.4362 (0.3491, 0.5646)	0.8704 (0.8260, 0.9141)	0.8102 (0.6680, 0.8692)	0.3387 (0.2778, 0.4478)	0.9273 (0.9050, 0.9424)
Bladder	0.4162 (0.2862, 0.5099)	0.6281 (0.3093, 0.7565)	0.8417 (0.7484, 0.9024)	0.4338 (0.2445, 0.7198)	0.6799 (0.4275, 0.7992)	0.9120 (0.8338, 0.9446)
Duodenum	0.1554 (0.1039, 0.2125)	0.3192 (0.2559, 0.3886)	0.5066 (0.4170, 0.5725)	0.3820 (0.2427, 0.4981)	0.3066 (0.2635, 0.3661)	0.7402 (0.6594, 0.7909)
Esophagus	0.2917 (0.1019, 0.6169)	0.3541 (0.2167, 0.5540)	0.5500 (0.4131, 0.6599)	0.5174 (0.3678, 0.6792)	0.3610 (0.2560, 0.5402)	0.7460 (0.6376, 0.8115)
Gallbladder	0.2831 (0.1756, 0.5198)	0.6161 (0.4809, 0.7200)	0.7999 (0.7097, 0.8725)	0.5643 (0.3615, 0.7377)	0.6609 (0.5446, 0.7245)	0.8763 (0.8020, 0.9082)
Left adrenal gland	0.0555 (0.0276, 0.2347)	0.4222 (0.3417, 0.4995)	0.5068 (0.3225, 0.6318)	0.4584 (0.3104, 0.6267)	0.3766 (0.3321, 0.4541)	0.7295 (0.6519, 0.7916)
Left kidney	0.8405 (0.6844, 0.9464)	0.8274 (0.7733, 0.8631)	0.9325 (0.8899, 0.9467)	0.8723 (0.7705, 0.9286)	0.7909 (0.7409, 0.8139)	0.9489 (0.9389, 0.9585)
Liver	0.7477 (0.6695, 0.8085)	0.5124 (0.4467, 0.5801)	0.6904 (0.5401, 0.8016)	0.8801 (0.8204, 0.9321)	0.6137 (0.5783, 0.6479)	0.9641 (0.9547, 0.9701)
Pancreas	0.2127 (0.1558, 0.3109)	0.3392 (0.2572, 0.4243)	0.5656 (0.5155, 0.6413)	0.5391 (0.3304, 0.7333)	0.3217 (0.2756, 0.4020)	0.8295 (0.7734, 0.8711)
Postcava	0.2042 (0.1402, 0.3478)	0.5251 (0.4349, 0.5925)	0.4436 (0.3029, 0.6463)	0.6683 (0.5353, 0.7672)	0.5211 (0.4598, 0.6180)	0.8384 (0.7909, 0.8684)
Prostate uterus	0.2344 (0.1655, 0.3081)	0.6986 (0.5430, 0.7522)	0.7518 (0.6567, 0.8261)	0.6231 (0.5330, 0.7364)	0.7739 (0.6685, 0.8271)	0.8557 (0.8255, 0.8901)
Right adrenal gland	0.0452 (0.0268, 0.1082)	0.3642 (0.2766, 0.4491)	0.1681 (0.0873, 0.3560)	0.3708 (0.2454, 0.5182)	0.3855 (0.3103, 0.4710)	0.6994 (0.6138, 0.7661)
Right kidney	0.8459 (0.5935, 0.9497)	0.8215 (0.7528, 0.8577)	0.9077 (0.8685, 0.9419)	0.8632 (0.7755, 0.9258)	0.7851 (0.7506, 0.8227)	0.9505 (0.9426, 0.9585)
Spleen	0.5936 (0.4686, 0.7846)	0.6536 (0.5934, 0.7697)	0.9267 (0.8821, 0.9483)	0.8591 (0.7552, 0.9297)	0.7038 (0.6609, 0.7766)	0.9589 (0.9465, 0.9677)
Stomach	0.4229 (0.3437, 0.5479)	0.3883 (0.3051, 0.4713)	0.5399 (0.4555, 0.6267)	0.4576 (0.2540, 0.6447)	0.4378 (0.3503, 0.5379)	0.9123 (0.8677, 0.9369)
ULS23(DeepLesion3D)	0.3686 (0.0855, 0.7680)	0.7473 (0.6817, 0.8063)	0.3258 (0.1325, 0.5707)	0.2386 (0.1045, 0.4372)	0.7680 (0.7103, 0.8160)	0.7065 (0.6247, 0.7782)
ULS23(Bone)	0.4461 (0.2349, 0.6676)	0.6671 (0.5854, 0.7443)	0.1947 (0.0898, 0.3969)	0.4447 (0.1481, 0.7026)	0.6896 (0.6128, 0.7530)	0.6920 (0.6097, 0.7702)
ULS23(Pancreas)	0.0675 (0.0471, 0.1237)	0.5579 (0.4911, 0.6111)	0.5548 (0.4862, 0.6382)	0.5526 (0.3287, 0.6786)	0.6561 (0.5857, 0.7143)	0.7265 (0.6722, 0.7776)

Note: Dice scores are displayed as Median values (First quartile, Third quartile).

Algorithm 1 SegVol training loop

Input: SegVol model, training image x , ground truth mask set $Y_x = \{y_i\}_{i=1}^n$, category set $S_x = \{s_i\}_{i=1}^n$, pseudo mask set $Z_x = \{z_i\}_{i=1}^m$

Output: SegVol Model parameters

```
1:  $n_{pt} \leftarrow 6$ 
2:  $\alpha \leftarrow 0.1$ 
3: # Loop for each category of this case.
4: for  $i \leftarrow 1$  to  $n$  do
5:    $f_{img} \leftarrow \text{model.ImageEncoder}(x)$ 
6:    $pt_{spatial} \leftarrow \text{prompt\_generate}(y_i)$ 
7:    $pt_{semantic} \leftarrow \text{TextTemplate}(s_i)$ 
8:    $l_{gt} \leftarrow 0$ 
9:   # Loop for possible prompt composite types of ground truth mask.
10:  for  $p \leftarrow 1$  to  $n_{pt}$  do
11:    # Choose one prompt composite type.
12:     $pt'_{spatial}, pt'_{semantic} \leftarrow \text{PromptStrategy}(pt_{spatial}, pt_{semantic})$ 
13:     $f_{text} \leftarrow \text{model.TextEncoder}(pt'_{semantic})$ 
14:     $f_{prompt} \leftarrow \text{model.PromptEncoder}(pt'_{spatial}, f_{text})$ 
15:     $pred_{gt} \leftarrow \text{model.Decoder}(f_{img}, f_{prompt}, f_{text})$ 
16:     $l_{gt} \leftarrow l_{gt} + \text{DiceLoss}(pred_{gt}, y_i) + \text{BCELoss}(pred_{gt}, y_i)$ 
17:  end for
18:   $l_{pseudo} \leftarrow 0$ 
19:  # Loop for several pseudo masks.
20:  for  $p \leftarrow 1$  to  $n_{pt}$  do
21:    # Random select a pseudo mask of this case for training.
22:     $z_p \leftarrow \text{RandomSelectInt}([1, m])$ 
23:     $pt_{spatial} \leftarrow \text{prompt\_generate}(z_p)$ 
24:     $f_{prompt} \leftarrow \text{model.PromptEncoder}(pt_{spatial})$ 
25:     $pred_{pseudo} \leftarrow \text{model.Decoder}(f_{img}, f_{prompt})$ 
26:     $l_{pseudo} \leftarrow l_{pseudo} + \text{DiceLoss}(pred_{pseudo}, z_p) + \text{BCELoss}(pred_{pseudo}, z_p)$ 
27:  end for
28:   $l \leftarrow l_{gt} + \alpha \times l_{pseudo}$ 
29:   $\text{update}(\text{model}, l)$ 
30: end for
31: return model
```

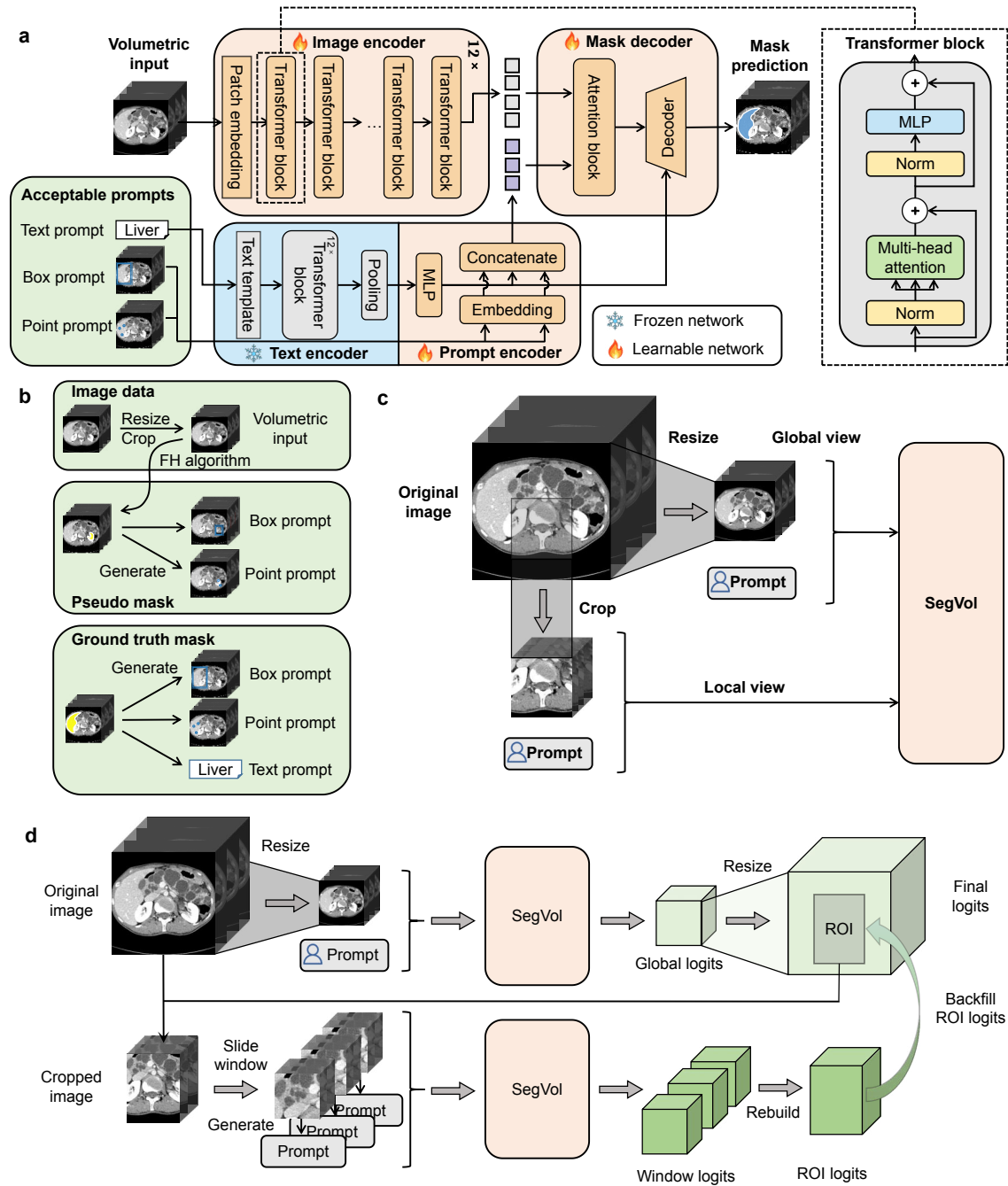


Figure 1. An overview of the model architecture of the proposed SegVol. **a** The main structure of SegVol includes the image encoder, text encoder, prompt encoder, and mask decoder. All networks, except the text encoder, are learnable. The image encoder extracts the image embedding of volumetric input. The image embedding is fed into the decoder together with prompt embeddings to predict the segmentation mask. **b** Illustration of input image transformation and the prompt generation. **c** Zoom-out-zoom-in training: SegVol is trained on data of both global and local views. **d** Zoom-out-zoom-in inference: SegVol first conducts global inference and then performs local inference on the extracted ROI to refine the results.

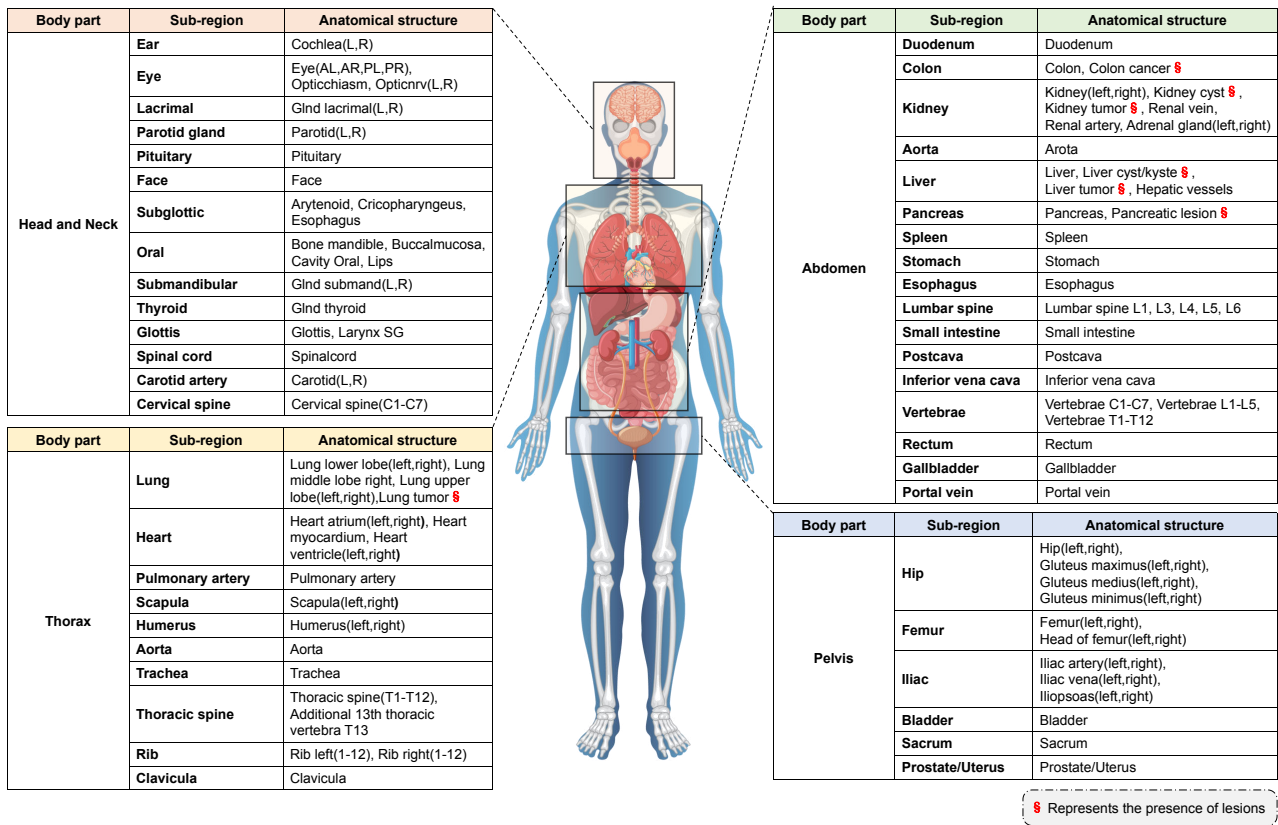


Figure 2. Overview of the joint supervised fine-tuning dataset. The joint dataset comprises 47 important regions, with each region containing one or multiple significant anatomical structures within that spatial area. Image of human body by brgfx on Freepik [3].

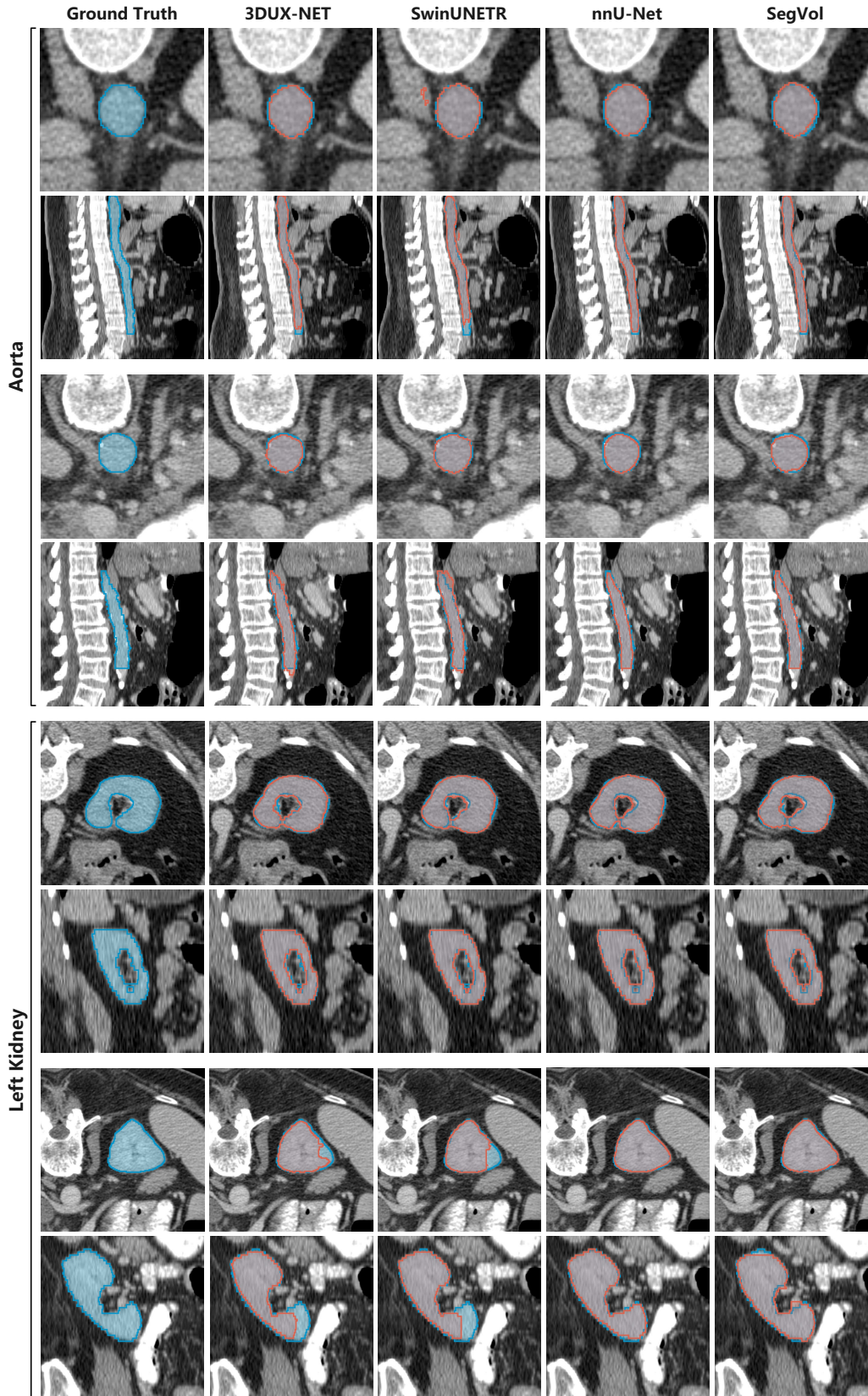


Figure 3. Visualized aorta and left kidney prediction results of 3DUX-NET [33], SwinUNETR [15], nnU-Net [24] and SegVol on 4 cases from internal validation set. For the integrality of aorta and left kidney structure modeling, SegVol significantly outperforms 3DUX-NET and SwinUNETR and is comparable to nnU-Net.

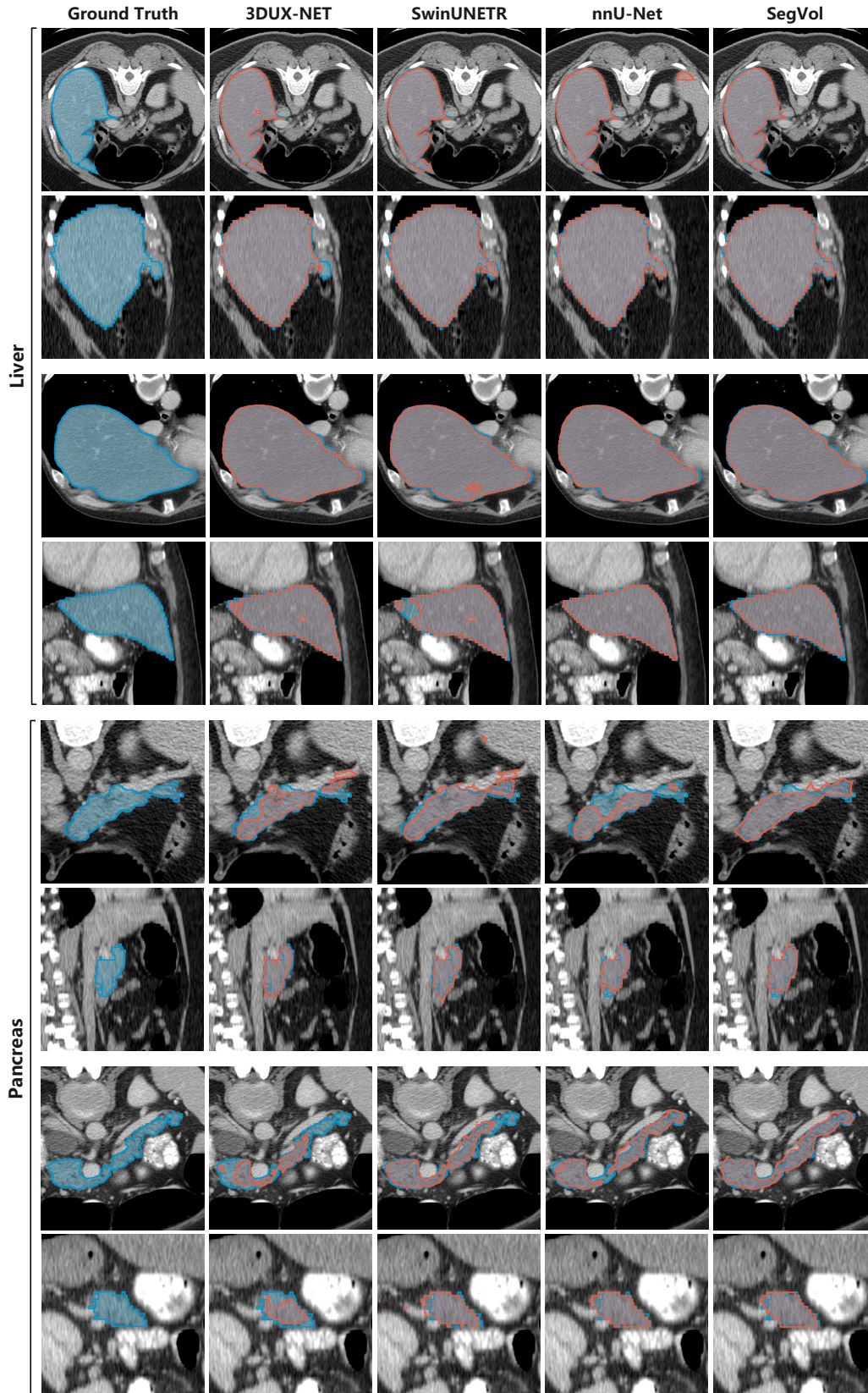


Figure 4. Visualized liver and pancreas prediction results of 3DUX-NET [33], SwinUNETR [15], nnU-Net [24] and SegVol on 4 cases from internal validation set. For the modeling of pancreas, SegVol is significantly superior to other baseline methods.

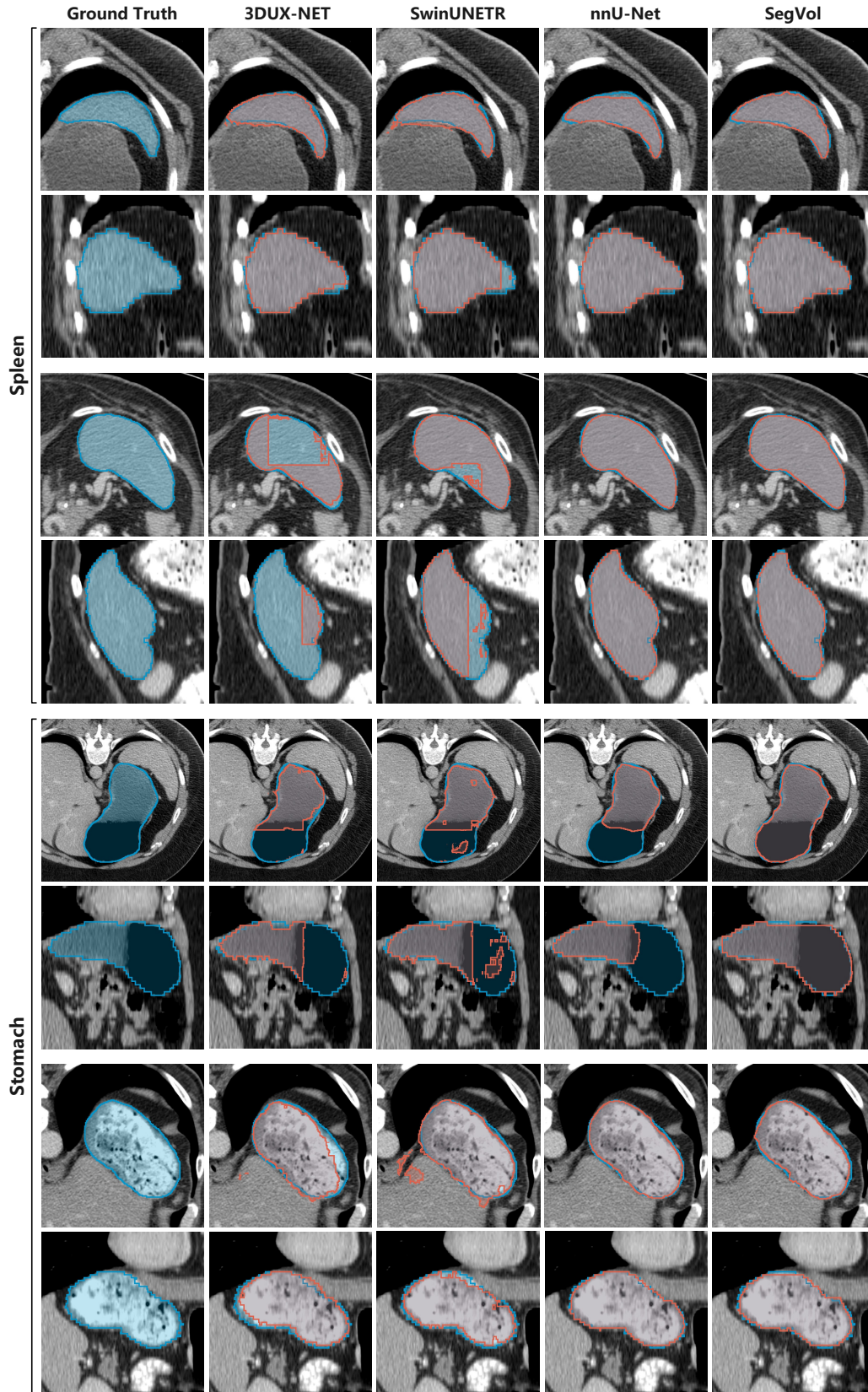


Figure 5. Visualized spleen and stomach prediction results of 3DUX-NET [33], SwinUNETR [15], nnU-Net [24] and SegVol on 4 cases from internal validation set. For the consistency and stability of stomach modeling, SegVol is significantly better than other methods.

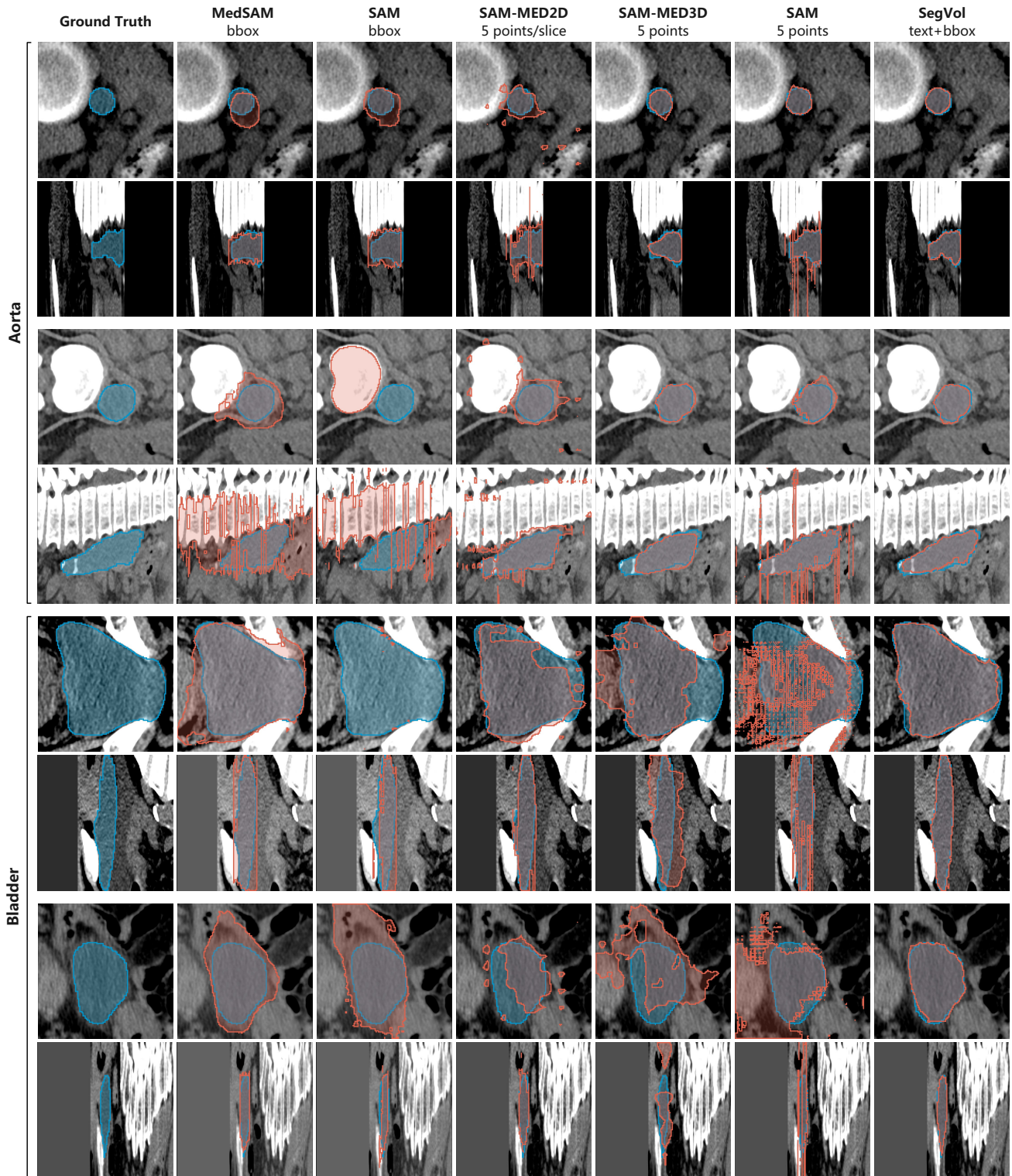


Figure 6. Visualized aorta and bladder prediction results of MedSAM [38], SAM(bbox) [31], SAM-MED2D [6], SAM-MED3D [64], SAM(points) [31] and SegVol on 4 cases from external validation set.

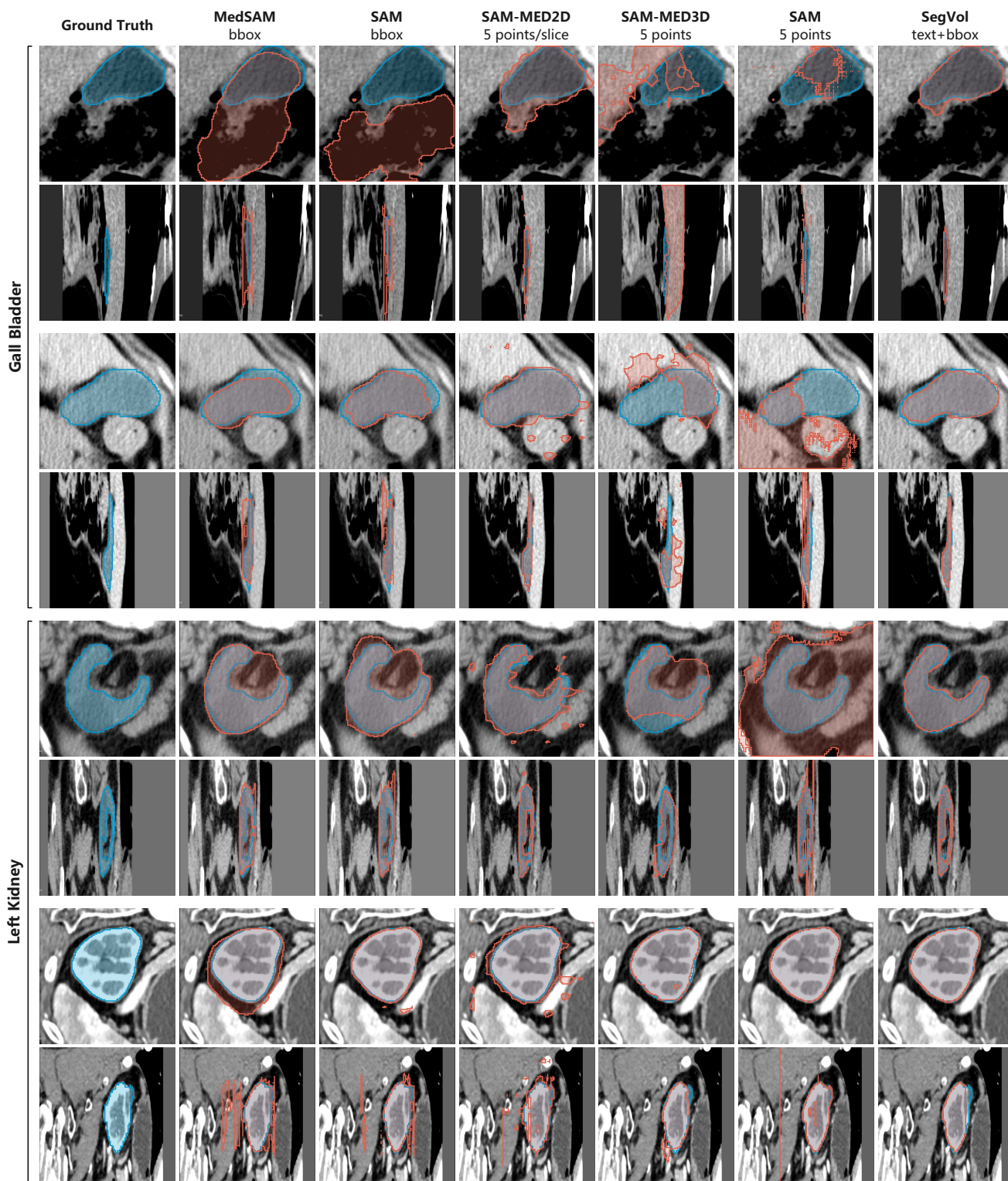


Figure 7. Visualized gall bladder and left kidney prediction results of MedSAM [38], SAM(bbox) [31], SAM-MED2D [6], SAM-MED3D [64], SAM(points) [31] and SegVol on 4 cases from external validation set.

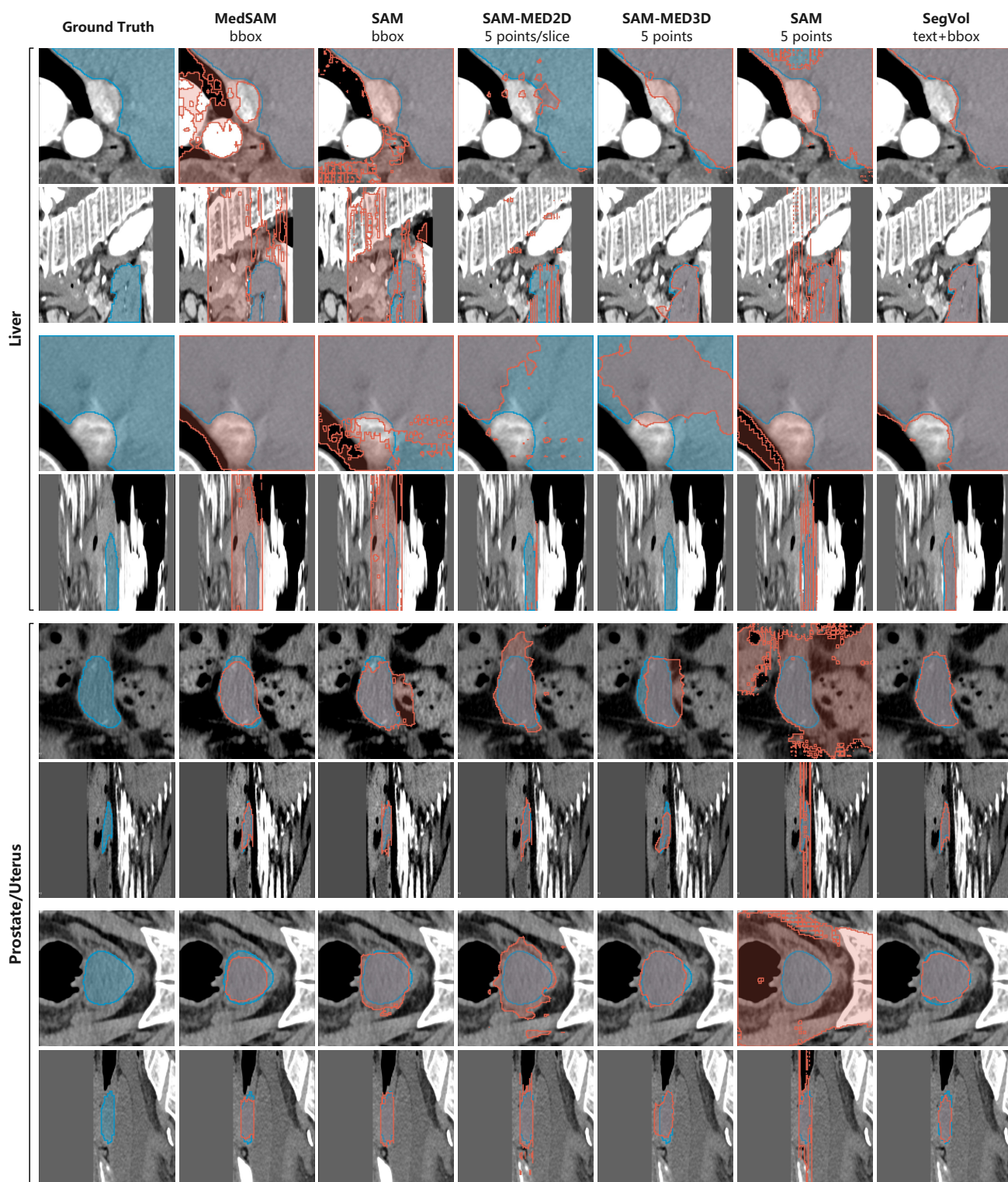


Figure 8. Visualized liver and prostate/uterus prediction results of MedSAM [38], SAM(bbox) [31], SAM-MED2D [6], SAM-MED3D [64], SAM(points) [31] and SegVol on 4 cases from external validation set.

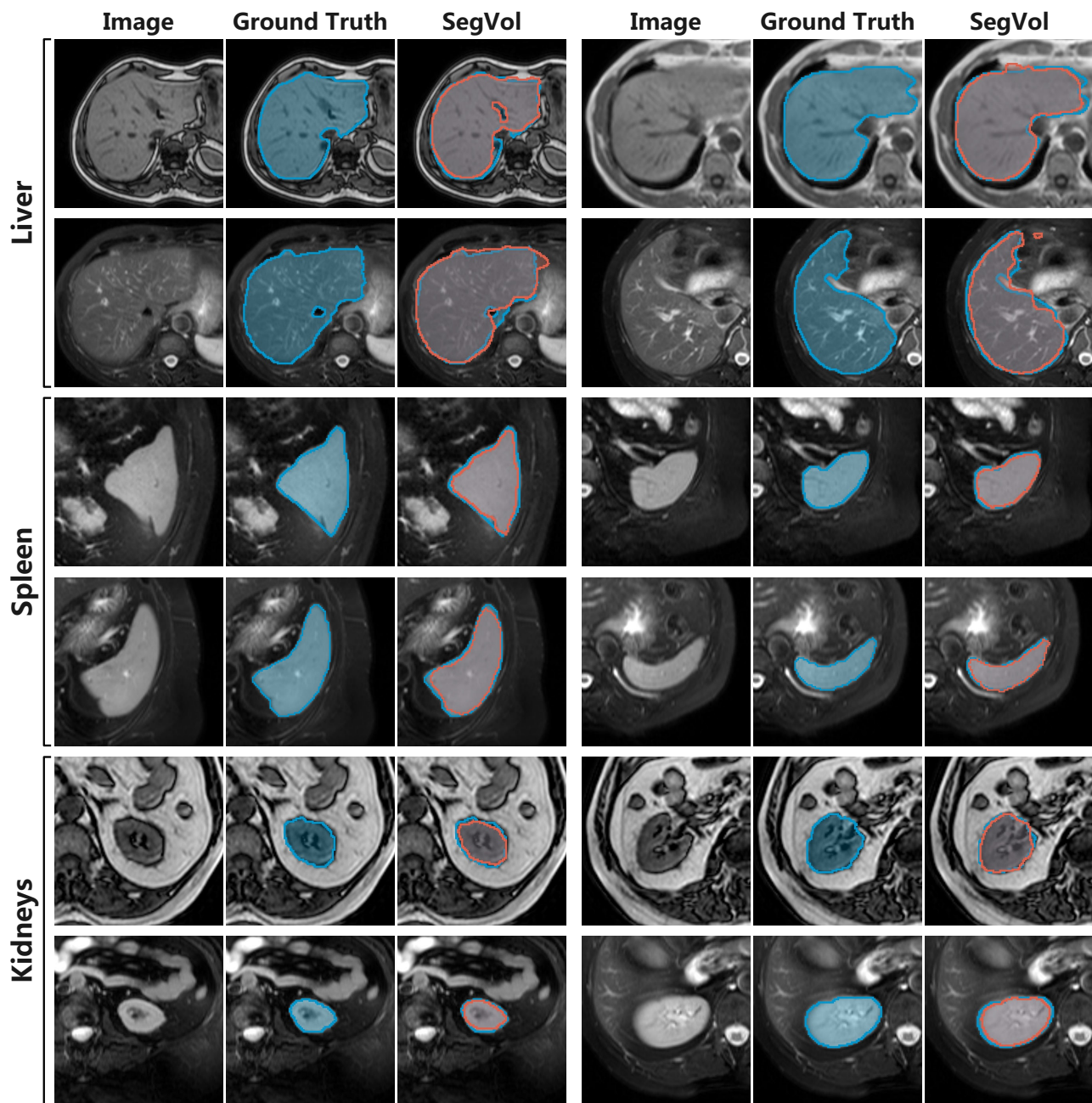


Figure 9. Visualized liver, spleen and kidney prediction results of SegVol on 12 cases from MRI set of CHAOS [28–30]. For unseen MRI modality, SegVol is still able to segment these four organs relatively accurately.